

# Synthesis, Structural, and Physicochemical Characterization of a $Ti_6$ and a Unique Type of $Zr_6$ Oxo Clusters Bearing an Electron-Rich Unsymmetrical {OON} Catechol/Oxime Ligand and Exhibiting Metalloaromaticity

Stamatis S. Passadis, Michael G. Papanikolaou, Alexander Elliott, Constantinos G. Tsiafoulis, Athanassios C. Tshipis,\* Anastasios D. Keramidas,\* Haralampos N. Miras,\* and Themistoklis A. Kabanos\*



Cite This: <https://dx.doi.org/10.1021/acs.inorgchem.0c02959>



Read Online

ACCESS |



Metrics & More

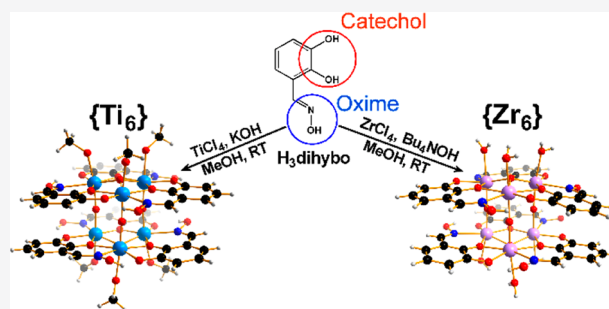


Article Recommendations



Supporting Information

**ABSTRACT:** The chelating catechol/oxime ligand 2,3-dihydroxybenzaldehyde oxime ( $H_3$ dihybo) has been used to synthesize one titanium(IV) and two zirconium(IV) compounds that have been characterized by single-crystal X-ray diffraction and  $^1H$  and  $^{13}C$  NMR, solid-state UV–vis, and ESI-MS spectroscopy. The reaction of  $TiCl_4$  with  $H_3$ dihybo and KOH in methanol, at ambient temperature, yielded the hexanuclear titanium(IV) compound  $K_2[Ti^{IV}_6(\mu_3-O)_2(\mu-O)_3(OCH_3)_4(CH_3OH)_2(\mu-Hdihybo)_6] \cdot CH_3OH$  (**1**), while the reaction of  $ZrCl_4$  with  $H_3$ dihybo and either  $nBu_4NOH$  or KOH also gave the hexanuclear zirconium(IV) compounds **2** and **3**, respectively. Compounds **1–3** have the same structural motif  $[M^{IV}_6(\mu_3-O)_2(\mu-O)_3]$  ( $M = Ti, Zr$ ), which constitutes a unique example with a trigonal-prismatic arrangement of the six zirconium atoms, in marked contrast to the octahedral arrangement of the six zirconium atoms in all the  $Zr_6$  clusters reported thus far, and a unique  $Zr_6$  core structure. Multinuclear NMR solution measurements in methanol and water proved that the hexanuclear clusters **1** and **3** retain their integrity. The marriage of the catechol moiety with the oxime group in the ligand  $H_3$ dihybo proved to be quite efficient in substantially reducing the band gaps of  $TiO_2$  and  $ZrO_2$  to 1.48 and 2.34 eV for the titanium and zirconium compounds **1** and **3**, respectively. The application of **1** and **3** in photocurrent responses was investigated. ESI-MS measurements of the clusters **1** and **3** revealed the existence of the hexanuclear metal core and also the initial formation of trinuclear  $M_3$  ( $M = Ti, Zr$ ) building blocks prior to their self-assembly into the hexanuclear  $M_6$  ( $M = Ti, Zr$ ) species. Density functional theory (DFT) calculations of the NICS<sub>zz</sub> scan curves of these systems revealed that the triangular  $M_3$  ( $M = Ti, Zr$ ) metallic ring cores exhibit pronounced metalloaromaticity. The latter depends upon the nature of the metallic center with NICS<sub>zz</sub>(1) values equal to  $-30$  and  $-42$  ppm for the Ti (compound **1**) and Zr (compound **2**) systems, respectively, comparable to the NICS<sub>zz</sub>(1) value of the benzene ring of  $-29.7$  ppm calculated at the same level of theory.



## INTRODUCTION

Polyoxo-titanium clusters (PTCs) have drawn unprecedented attention<sup>1</sup> over the last few years due to their potential applications in photocatalytic hydrogen production,<sup>2</sup> in solar energy conversion,<sup>3</sup> in the degradation of environmental pollutants,<sup>4</sup> and in the reduction of carbon dioxide.<sup>5</sup>

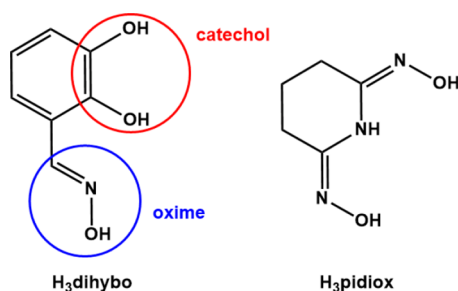
The precise knowledge of the structures of PTCs, since these oxide clusters are soluble analogues of discrete fragments of solid  $TiO_2$ , originates from the necessity to understand the binding modes of sensitizers to  $Ti-O$  surfaces.<sup>6</sup> The large band gap (3.20 eV) of anatase ( $TiO_2$ ) limits its applications in photocatalysis.<sup>7</sup> The employment of organic chelators could allow the manipulation of the band gap and presumably the subsequent visible light absorption by PTCs.<sup>8</sup>

In a similar manner, zirconium dioxide has been used in a wide range of applications such as the degradation of organic pollutants,<sup>9</sup> as well as in photochemical water splitting,<sup>10</sup> fuel cells,<sup>11</sup> and photocatalysis.<sup>12</sup> The band gap of  $ZrO_2$  ranges from 3.25 to 5.1 eV depending on its phase and the method of its preparation.<sup>13</sup> Moreover, the field of zirconium-based MOFs has exploded in the last few years.<sup>14</sup>

Received: October 7, 2020

Previous studies demonstrated the strong chelating affinity of catechol toward high-oxidation-state metals.<sup>15</sup> Additionally, oximes<sup>16</sup> are also strong binders to the group IV transition metals in their highest oxidation state. Thus, it was envisaged that the incorporation of both functional groups within the same chelating system as in the case of 2,3-dihydroxybenzaldehyde oxime ( $H_3$ dihybo, Scheme 1)<sup>17</sup> could potentially allow us to exploit the structural and electronic effects of both groups and modulate the material's band gap.

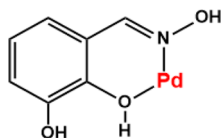
**Scheme 1. Ligands  $H_3$ dihybo and  $H_3$ pidiox**



Research on the band gap tuning of TOCs, via a dye sensitization method, is an important topic and the marriage of the catechol moiety with the oxime group in neighboring positions in the  $H_3$ dihybo (Scheme 1) ligand would lead to a substantial reduction of the  $TiO_2$  and  $ZrO_2$  band gaps.

Moreover, the presence of the electron-withdrawing  $-C=N-OH$  group on the aromatic ring is predicted to significantly lower the catechol protonation constant, making it a much more effective sequestering ligand at neutral or even acidic pH values. Here we demonstrate for the first time the effective use of the  $H_3$ dihybo ligand for the construction of multinuclear clusters, allowing the modulation of the cluster's band gap and the induction of metalloaromaticity effects. The ligand's chelating ability has been reported only once in the case of a palladium(0) monomeric complex,<sup>17c</sup>  $[Pd^0(H_3dihybo)]$ , where its structure (Scheme 2) has been proposed only on the basis of NMR and IR data.

**Scheme 2. Proposed Structure of the Palladium(0) Complex  $[Pd^0(H_3dihybo)]$  on the Basis of IR and NMR Data**



Furthermore, the ligand  $H_3$ dihybo, which also exhibits donor atoms in three neighboring positions of the ring, in a fashion similar to that for the ligand  $H_3$ pidiox<sup>16a</sup> (Scheme 1) gave rise to the formation of a PTC containing two *cyclo*- $Ti_3$  metallic cores exhibiting metalloaromaticity. Metalloaromaticity is a relatively new concept used to describe the aromaticity of all-metal rings<sup>18</sup> with potential applications in molecular electronics.<sup>19a</sup> Additionally, the emergence of metalloaromaticity in metals, metal oxides, and mixed-metal clusters is of vital importance in explaining the chemical bonding as well as understanding the electronic and surface properties of the metals, metal oxides, and metal alloys.<sup>19b</sup> The mixed metal Al–Li forms a strong and lightweight material which has been used extensively in aerospace engineering.<sup>19c</sup> The ongoing research in this field

revealed quite a few examples of compounds bearing all-metal-based aromatic rings and that were characterized as being metalloaromatic. The most popular aromaticity/antiaromaticity criteria are based on structural (ring planarity), energetic (aromatic stabilization energy, ASE), magnetic (paratropicity/diatropicity), and electronic (electron delocalization descriptors) properties. As far as the electronic delocalization descriptors are concerned, the aromaticity of organic compounds arises from electron delocalization supported by the formation of  $\pi$  MOs ( $\pi$ -type aromaticity), while in all-metal aromatic rings electron delocalization could take place through the formation of  $\sigma$ ,  $\pi$ ,  $\delta$ , and  $\varphi$  MOs. The aromaticities of three-, four-, five-, and six-membered metal rings have been extensively studied.<sup>18d</sup> For example, it has been reported<sup>18c</sup> that the  $[c-X_3]^-$  ( $X = B, Al, Ga$ ) “bare” metallic rings exhibit double ( $\sigma + \pi$ ) aromaticity. Other examples of three-membered aromatic metallic rings are the “ligand stabilized” *cyclo*- $M_3(\mu-H)_3$  ( $M = Cu, Ag, Au$ ) systems.<sup>18d</sup> Similar studies have also reported aromaticity for the “bare” four-membered ring in  $[c-Al_4]^-$  as well for the “ligand stabilized”  $[M_4(CO)_{12}]$  ( $M = Fe, Ru, Os$ ) systems.<sup>18f</sup> Similarly, many studies of five- and six-membered metallic rings have also been reported.<sup>18d</sup>

We employed herein almost the full range of aromaticity descriptors, including structural and magnetic descriptors (particularly the most powerful descriptor, the nucleus-independent chemical shift (NICS)) in an effort to investigate the system's behavior.<sup>20</sup> The NICS has been widely applied as a magnetic criterion of the aromaticity of organic rings (e.g., the NICS of the archetypic benzene molecule at the ring center, NICS(0), is  $-9.7$  ppm).<sup>21</sup> Note that comparable or even higher NICS(0) values have been theoretically estimated for all-metal rings.<sup>18d</sup>

In this contribution, we report the successful synthesis of three hexanuclear polyoxometalates of the general formula  $[M^{IV}_6(\mu_3-O)_2(\mu-O)_3(\mu-\eta^1, \eta^2, \eta^1-Hdihybo-O, O', N)_6]$  ( $M = Ti, Zr$ ) by reacting  $MCl_4$  ( $M = Ti, Zr$ ) with  $H_3$ dihybo in the presence of either KOH or  $nBu_4NOH$  as a base in methanol at room temperature. The three compounds were characterized by single-crystal X-ray structure analysis and various physicochemical techniques. Not only the core structure of the zirconium compounds  $[Zr_6(\mu_3-O)_2(\mu-O)_3]$  but also the trigonal-prismatic arrangement of the six zirconium atoms are unique. The *cyclo*- $M_3$  ( $M = Ti, Zr$ ) metallic cores exhibit metalloaromaticity. The band gap investigation of the compounds showed a very low values of 1.48 and 2.34 eV for the titanium (1) and zirconium (3) compounds, respectively.

## EXPERIMENTAL SECTION

**Materials, Syntheses, and Physical Measurements.** All chemicals and solvents were purchased from Sigma-Aldrich and Merck, were of reagent grade, and were used without further purification, except  $TiCl_4$ , which was distilled under high vacuum just prior to use. Merck silica gel 60 F254 TLC plates were used for thin-layer chromatography. C, H, and N analyses were conducted by the microanalytical service of the School of Chemistry, the University of Glasgow. FT-IR transmission spectra of the compounds, in KBr pellets, were acquired using a JASCO Model 460 spectrophotometer in the  $4000-400$   $cm^{-1}$  range. The UV–vis diffuse reflectance spectra were recorded at room temperature on an Agilent Cary 60 UV–vis spectrophotometer.

**Synthesis of the Organic Molecule 2,3-Dihydroxybenzaldehyde Oxime ( $H_3$ dihybo).** To a stirred anhydrous ethanol solution (30 mL) containing NaOH (0.694 g, 17.37 mmol) and  $NH_2OH \cdot HCl$  (1.207 g, 17.37 mmol) was added in one portion solid 2,3-

dihydroxybenzaldehyde (1.500 g, 10.86 mmol). The reaction mixture was refluxed for 3 h under argon. Then, the solvent was evaporated to dryness under high vacuum to give a crude light brown mixture. Dichloromethane (50 mL) was added to the solid, and the solution was refluxed for 10 min under argon. The boiling solution was filtered and cooled first to room temperature ( $\sim 20$  °C) and then to 4 °C for 1 h, during which period white crystals of the desired product were formed. The crystals were filtered and dried under vacuum to yield 1.33 g of H<sub>3</sub>dihydro. Yield: 80% (based on 2,3-dihydroxybenzaldehyde). Mp: 113 °C. High-resolution electrospray ionization mass spectrometry (+) [HR-ESI(+)]-MS: calcd for C<sub>7</sub>H<sub>8</sub>NO<sub>3</sub> ([M + H]<sup>+</sup>) 154.0504, found 154.0503. Anal. Calcd for C<sub>7</sub>H<sub>8</sub>NO<sub>3</sub> (M<sub>r</sub> = 153.137): C, 54.88; H, 4.61; N, 9.15. Found: C, 54.90; H, 4.59; N, 9.13. R<sub>f</sub> = 0.06 (CHCl<sub>3</sub>/C<sub>6</sub>H<sub>14</sub> 4/1).

**Synthesis of K<sub>2</sub>[Ti<sup>IV</sup>(μ<sub>3</sub>-O)<sub>2</sub>(μ-O)<sub>3</sub>(OCH<sub>3</sub>)<sub>4</sub>(HOCH<sub>3</sub>)<sub>2</sub>(μ-η<sup>1</sup>,η<sup>2</sup>,η<sup>1</sup>-Hdihydro-O,O',N)<sub>6</sub>·CH<sub>3</sub>OH (1).** To a stirred methyl alcohol solution (4 mL) were successively added H<sub>3</sub>dihydro (69.8 mg, 0.456 mmol) and TiCl<sub>4</sub> (0.05 mL, 86.5 mg, 0.456 mmol). The colorless solution of the ligand turned dark red upon addition of TiCl<sub>4</sub>. Then, addition of solid KOH (51.1 mg, 0.912 mmol) in one portion resulted in the formation of a small quantity of precipitate. The solution was kept overnight at  $\sim 4$  °C (to remove most of the formed KCl); the mixture was filtered off, and the dark red filtrate was kept at room temperature ( $\sim 20$  °C) for 3–4 days, during which period of time 77.0 mg of dark red crystals of compound **1** were formed. The crystals were filtered off and dried under an ambient atmosphere. Yield: 65% (based on H<sub>3</sub>dihydro). Anal. Calcd for (C<sub>48</sub>H<sub>56</sub>N<sub>6</sub>O<sub>29</sub>K<sub>2</sub>Ti<sub>6</sub>·CH<sub>3</sub>OH, M<sub>r</sub> = 1572.381 g mol<sup>-1</sup>): C, 37.41; H, 3.46; N, 5.35. Found: C, 37.25; H, 3.57; N, 5.25.

**Synthesis of [Zr<sup>IV</sup>(μ<sub>3</sub>-O)<sub>2</sub>(μ-O)<sub>3</sub>(μ-η<sup>1</sup>,η<sup>2</sup>,η<sup>1</sup>-Hdihydro-O,O',N)<sub>6</sub>(OH<sub>2</sub>)<sub>6</sub>]Cl<sub>2</sub>·2Bu<sub>4</sub>NCl·2CH<sub>3</sub>OH (2).** To a stirred methyl alcohol solution (2 mL) were successively added 2,3-dihydroxybenzaldehyde oxime (65.7 mg, 0.429 mmol), and ZrCl<sub>4</sub> (100.0 mg, 0.429 mmol). The colorless solution of the ligand turned orange upon addition of ZrCl<sub>4</sub>. Then, the addition of 2.20 mL of tetrabutylammonium hydroxide, 0.39 M in methyl alcohol (222.0 mg, 0.858 mmol) in one portion, caused the formation of small amount of a white precipitate, which was filtered off. The light orange filtrate was kept at room temperature ( $\sim 20$  °C) for 3–4 days, during which period yellow crystals of compound **2** were formed. We were unable to prepare an analytically pure sample on a preparative scale because compound **2** is very hygroscopic.

**Synthesis of [Zr<sup>IV</sup>(μ<sub>3</sub>-O)<sub>2</sub>(μ-O)<sub>3</sub>(μ-η<sup>1</sup>,η<sup>2</sup>,η<sup>1</sup>-Hdihydro-O,O',N)<sub>6</sub>(OCH<sub>3</sub>)<sub>2</sub>(OH<sub>2</sub>)<sub>4</sub>]·2CH<sub>3</sub>OH (3).** To a stirred methyl alcohol solution (4.0 mL) were successively added 2,3-dihydroxybenzaldehyde oxime (65.7 mg, 0.429 mmol), ZrCl<sub>4</sub> (100.0 mg, 0.429 mmol), and KOH (48.1 mg, 0.858 mmol). Upon addition of KOH a small amount of a white precipitate was formed. The solution was kept overnight at  $\sim 4$  °C to remove most of the formed KCl, which was filtered off. The light orange filtrate was kept at room temperature ( $\sim 20$  °C) for 3–4 days, during which period 45 mg of yellow crystals of compound **3** were formed. The crystals were filtered off and dried under an ambient atmosphere. Yield: 37% (based on H<sub>3</sub>dihydro). Anal. Calcd for (C<sub>44</sub>H<sub>44</sub>N<sub>6</sub>O<sub>29</sub>Zr<sub>6</sub>·2CH<sub>3</sub>OH, M<sub>r</sub> = 1732.28 g mol<sup>-1</sup>): C, 31.89; H, 2.96; N, 4.85. Found: C, 31.93; H, 3.15; N, 4.80.

**X-ray Crystallography.** A suitable single crystal was selected and mounted onto a rubber loop using Fomblin oil. Single-crystal X-ray diffraction data of **1–3** were recorded on a Bruker Apex CCD diffractometer ( $\lambda(\text{Mo K}\alpha) = 0.71073$  Å) at 150 K equipped with a graphite monochromator. Structure solution and refinement were carried out with SHELXS-97<sup>22</sup> and SHELXL-97<sup>23</sup> using the WinGX software package.<sup>24</sup> Data collection and reduction were performed using the Apex2 software package. Corrections for incident and diffracted beam absorption effects were applied using empirical absorption corrections.<sup>25</sup> All of the other atoms and most of the carbon atoms were refined anisotropically. Solvent molecule sites were found and included in the refinement of the structures. Multiple crystallization efforts allowed us to obtain single crystals and subsequent data collection of compound **3**. However, the poor quality of the single crystal led to a structure solution with a slightly elevated R

factor. Final unit cell data and refinement statistics for compounds **1–3** are collated in Table S1.

**NMR Analysis.** A sample solution was transferred into a 5 mm NMR tube. NMR experiments were performed on a Bruker AV500 spectrometer (Bruker Biospin, Rheinstetten, Germany) at 298 K using the Topspin 2.1 suite. All 1D <sup>1</sup>H NMR spectra were collected using a 30° flip angle, a spectral width of 14 ppm, a relaxation delay of 5 s, and an acquisition time of 4.3 s. A total of 64 K data points were collected, and the FIDs were treated using a line-broadening exponential function of 0.3 Hz. Phase adjustment and baseline correction were carried out using the Topspin 2.1 suite. Signal integration was performed manually.

2D <sup>1</sup>H–<sup>1</sup>H TOCSY, <sup>1</sup>H–<sup>13</sup>C HSQC, and <sup>1</sup>H–<sup>13</sup>C HMBC NMR experiments were recorded using standard Bruker software. T<sub>1</sub> measurements were obtained by using the inversion recovery method. The 2D <sup>1</sup>H–<sup>1</sup>H TOCSY experiments were measured using 256 increments of 2 K size (each consisting of 33 scans) covering the full spectrum (10 ppm in both dimensions). The standard grNOESY pulse sequence was used in the 2D <sup>1</sup>H–<sup>1</sup>H grEXSY-grNOESY measurements. These spectra were acquired using 512 increments of 2 K size (with 60 scans each) covering the full spectrum (10 ppm in both dimensions) or partial (3–4 ppm) regions of the spectrum. The delay time used in the 2D spectra was 3.0 s, on the basis of the measured T<sub>1</sub> values. Variable mixing times ranging from 0 to 0.1 s were used. <sup>1</sup>H–<sup>13</sup>C grHSQC and <sup>1</sup>H–<sup>13</sup>C grHMBC NMR experiments were measured using 512 increments of 2 K size (each consisting of 40 scans) covering the full spectrum (10 ppm at f2 and 160 ppm (HSQC) and 220 ppm (HMBC) at f1 dimensions). All NMR samples were prepared by dissolving the crystalline compounds in CD<sub>3</sub>OD at room temperature.

**Photocurrent Measurements.** The photocurrent measurements of compounds **1** and **3** were carried out on FTO electrodes by drop-casting solutions of the clusters of appropriate concentrations according to the following procedure. Crystals (5 mg) of compounds **1** and **3** were dissolved in 2 mL of methanol. A 0.2 μL portion of the prepared solutions was drop-casted onto a fluorine-doped indium–tin oxide (FTO) glass (2.5 × 5 cm). After evaporation under an ambient atmosphere, the coated film was used as the working electrode. Photocurrent measurements were conducted using a CHI 760E electrochemical workstation in a three-electrode system, with an Ag/AgCl electrode as the reference electrode and a Pt wire as the auxiliary electrode. All of the tests were performed at the same bias potential of +0.4 V, and an aqueous solution of Na<sub>2</sub>SO<sub>4</sub> (0.1 mol L<sup>-1</sup>) was used as the electrolyte. A 250 W high-pressure xenon lamp was used as a full-wavelength light source, located 10 cm away from the FTO electrode. The on–off irradiation intervals were 10 s.

**ESI Mass Spectrometry.** All MS data were collected using a Q-trap, time-of-flight MS (Maxis Impact MS) instrument supplied by Bruker Daltonics Ltd. The detector was a time-of-flight, microchannel plate detector, and all data were processed using the Bruker Daltonics Data Analysis 4.1 software, while simulated isotope patterns were investigated using Bruker Isotope Pattern software and Molecular Weight Calculator 6.45. The calibration solution used was an Agilent ES tuning mix solution, Recorder No. G2421A, enabling calibration between approximately *m/z* 100 and 3000. This solution was diluted 60/1 with MeCN. Samples were dissolved in MeOH and introduced into the MS via direct injection at 180 μL h<sup>-1</sup>. The ion polarity for all MS scans recorded was negative, at 180 °C, with the voltage of the capillary tip set at 4000 V, the end plate offset at –500 V, the funnel 1 RF at 300 Vpp, and the funnel 2 RF at 400 Vpp.

**Computational Details.** The NICS<sub>zz</sub> scan curve was calculated using Cartesian coordinates obtained from the X-ray structure of the compounds as well from the model compounds employing the GIAO (gauge-including atomic orbitals) DFT method<sup>26,27</sup> as implemented in the Gaussian09 series of programs<sup>28</sup> using the PBE0 functional in combination with the 6-31G(d,p) and the Def2-TZVP basis sets for the nonmetal and the Ti and Zr metal atoms, respectively. The computational protocol will henceforth be denoted as GIAO/PBE0/Def2-TZVP(M)U6-31G(d,p)(E).

## RESULTS AND DISCUSSION

**Synthesis of the Ligand H<sub>3</sub>dihybo and Its Ti and Zr Hexanuclear Compounds.** The ligand H<sub>3</sub>dihybo was prepared via oximation of 2,3-dihydroxybenzaldehyde. The synthesis was carried out under argon to avoid the oxidation of the free hydroxylamine and the ligand. The organic molecule H<sub>3</sub>dihybo was synthesized following a modified version of the reported procedure<sup>17</sup> to avoid some unnecessary steps. The completion of the reaction was determined by TLC. The extraction of the crude H<sub>3</sub>dihybo with dichloromethane proved to be an effective purification method.

The hexanuclear Ti<sub>6</sub> cluster **1** was prepared by reacting the ligand H<sub>3</sub>dihybo (1 equiv) with TiCl<sub>4</sub> (1 equiv, distilled just prior to its use) and KOH (2 equiv) in methanol. Dark red crystals of **1** were formed after slow evaporation of the methanol (3 days) at ambient temperature (~20 °C). The hexanuclear Zr<sub>6</sub> clusters **2** and **3** were prepared according to the procedure for **1** using ZrCl<sub>4</sub> instead of TiCl<sub>4</sub> and Bu<sub>4</sub>NOH and KOH as bases for the synthesis of **2** and **3**, respectively.

**Crystal Structures.** Single-crystal X-ray diffraction analysis revealed that compounds **1–3** have the same structural motif (Figures 1, 2A, and 3, respectively, for **1–3**), and thus, the

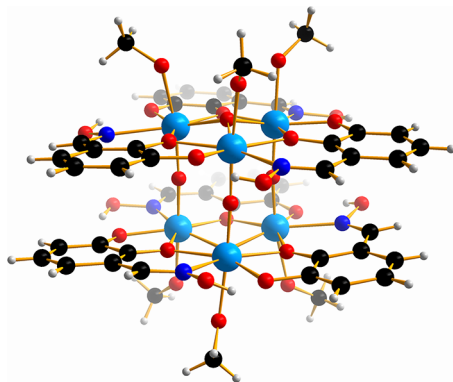


Figure 1. Ball-and-stick plot of the anion of **1**.

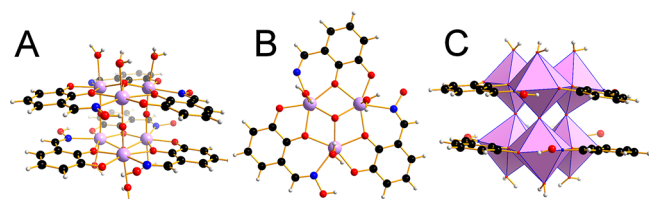


Figure 2. Ball-and-stick plot of the cation of **2** (A). Ball-and-stick plot of the structural unit  $[\text{Zr}_3(\mu_3\text{-O})(\mu\text{-}\eta^1:\eta^2:\eta^1\text{-Hdihybo-O,O',N})_3(\text{OH}_2)_3]$  (B). Polyhedral/ball-and-stick representation of the cation of **2** (C).

structure of compound **2** will be reported in detail. The centrosymmetric structure of compound **2** consists of six zirconium atoms, three  $\mu_3\text{-O}$ , two  $\mu_3\text{-O}$ , and six  $(\mu\text{-}\eta^1:\eta^2:\eta^1\text{-Hdihybo}^{2-})$  ligands (Figure 2B and Scheme 3), and six terminal water molecules. The six zirconium atoms are seven-coordinate, with an NO<sub>6</sub> coordination environment in a pentagonal-bipyramidal arrangement. The three edge-sharing zirconium atoms, via  $\mu_3\text{-O}$  and a  $\mu\text{-O}_{\text{phenoxy}}$  atoms (Figure 2B), are linked by one  $\mu_3\text{-O}$  atom to generate a Zr<sub>3</sub>( $\mu_3\text{-O}$ ) subunit. The two Zr<sub>3</sub>( $\mu_3\text{-O}$ ) subunits, featuring a pyramidal mode, are connected by three O<sup>2-</sup> atoms via a vertex-sharing mode to form a Zr<sub>6</sub>O<sub>5</sub> core structure (Figure 2C). The symmetry-related  $\mu_3\text{-O}$  atoms in the two Zr<sub>3</sub>( $\mu_3\text{-O}$ ) subunits are 0.501(3) Å above the plane

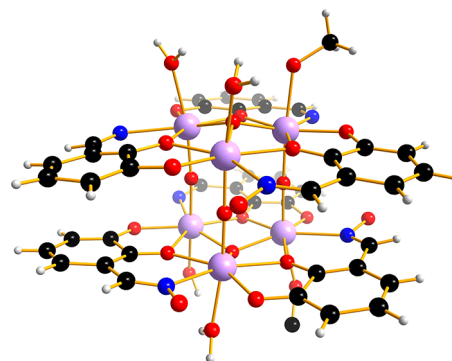
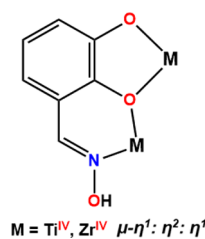


Figure 3. Ball-and-stick plot of compound **3**. Solvent molecules have been omitted for clarity.

### Scheme 3. Coordination Mode of the Ligand Hdihybo<sup>2-</sup> in Compounds **1–3**



defined by the Zr<sub>3</sub> structural unit. The Zr–( $\mu_3\text{-O}$ ) bond lengths (2.061(4)–2.072(4) Å, average 2.067 Å) and the Zr–( $\mu\text{-O}$ ) bond lengths (2.204(4)–2.231(4) Å, average 2.217 Å) are similar to those reported in the literature.<sup>29,30</sup>

The Zr...Zr distances in the symmetry-related structural units Zr<sub>3</sub>( $\mu_3\text{-O}$ ) (3.471(1)–3.481(1) Å, average 3.474 Å) are longer than those observed in  $[\{(\text{EtMe}_4\text{C}_5)\text{Zr}^{\text{IV}}\}_6(\mu_6\text{-O})(\mu_3\text{-O})_8]\cdot\text{C}_7\text{H}_8$ <sup>31</sup> (3.1542(9)–3.1709(11) Å, average 3.1645 Å) but shorter than those in  $[\{(\text{Cp}^*\text{Zr}^{\text{IV}})_6(\mu_4\text{-O})(\mu\text{-O})_4(\mu\text{-OH})_8\}]\cdot 2\text{C}_7\text{H}_8$ <sup>32</sup> (3.564(1)–3.608(1) Å, average 3.586 Å). The three angles in the symmetry-related Zr<sub>3</sub> triangles are almost 60°, and thus, it is obvious that the Zr<sub>3</sub> triangles are equilateral in a manner similar to the Ti<sub>3</sub>-based triangles observed in **1**. The  $d[\text{Zr}^{\text{IV}}\text{-O}_{\text{cat}}]_{\text{av}}$  and  $d[\text{Zr}^{\text{IV}}\text{-}(\mu\text{-O}_{\text{cat}})]_{\text{av}}$  values are 2.120(4) and 2.217(4) Å, respectively, and are very close to those reported in the literature.<sup>33</sup> The deprotonated catecholate moiety adopts a singly bridging chelate  $\mu\text{-}(\text{O},\text{O}',\text{O}')$  mode.<sup>33</sup> The  $d[\text{Zr}^{\text{IV}}\text{-N}_{\text{ox}}]_{\text{av}}$  value of 2.384(6) Å is much longer in comparison to the reported value of ~2.20 Å,<sup>34</sup> but in the latter case the oxime is deprotonated. Compound **2** is the first example of a polyoxo-catecholate zirconium compound to be reported.

All of the Zr<sup>IV</sup><sub>6</sub> discrete polyoxo clusters in the only three different Zr<sub>6</sub> core structures ( $[\text{Zr}^{\text{IV}}_6(\mu_6\text{-O})(\mu_3\text{-O})_8]$ ,<sup>24</sup>  $[\text{Zr}^{\text{IV}}_6(\mu_4\text{-O})(\mu\text{-O})_4(\mu\text{-OH})_8]$ ,<sup>32</sup> and  $[\text{Zr}^{\text{IV}}_6(\mu_3\text{-O})_4(\mu_3\text{-OH})_4]$ <sup>35</sup>) reported thus far have the six zirconium atoms in an octahedral arrangement. An octahedral Zr<sub>6</sub> arrangement has also been observed in the Zr<sup>IV</sup><sub>6</sub>-MOFs.<sup>14</sup> Thus, the Zr<sub>6</sub> discrete polyoxo cluster  $[\text{Zr}^{\text{IV}}_6(\mu_3\text{-O})_2(\mu\text{-O})_3]$  of this study is a unique example with a trigonal-prismatic arrangement of the six zirconium atoms and a unique Zr<sub>6</sub> core structure.

In marked contrast to the missing polyoxo-catecholate zirconium clusters, there are a few examples of polyoxo-catecholate titanium clusters.<sup>1b,3b,36</sup> In these polyoxo-titanium catecholate clusters the main binding modes of the deprotonated catecholate moiety are the singly bridging chelate  $\mu\text{-}(\text{O},\text{O}',\text{O}')$  and the singly bridging  $\mu\text{-}(\text{O},\text{O}')$ .

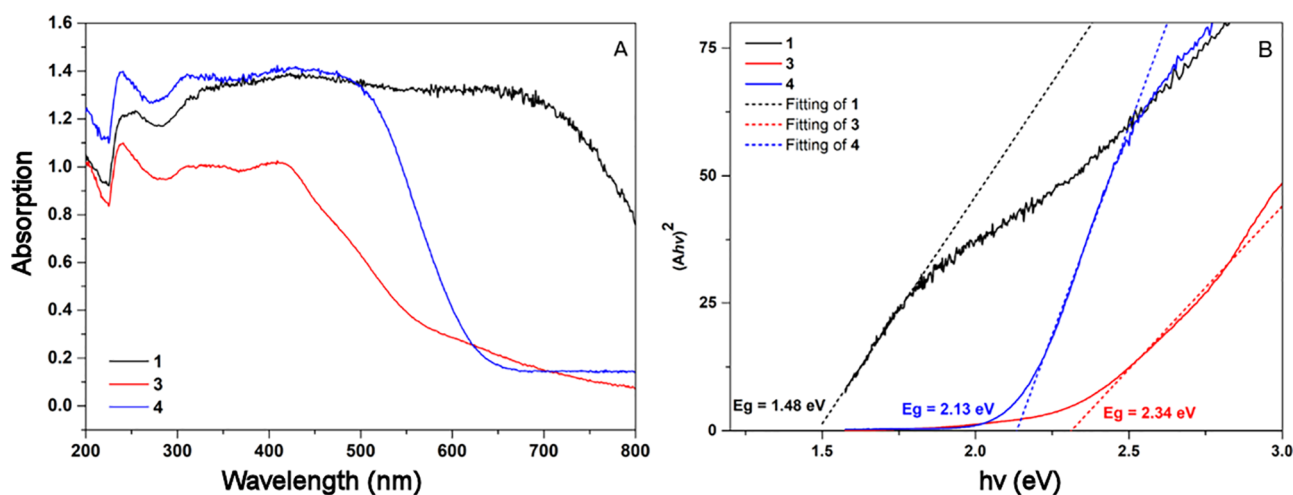


Figure 4. Solid-state UV-vis-NIR spectra of compounds 1, 3, and 4 (A). Tauc plots of compounds 1, 3 and 4 (B).

A comparison of the metrical parameters of the titanium cluster 1 with those of the zirconium cluster 2 reveals the following. In the case of the titanium isostructural cluster 1 the  $Ti_6$  metallic core appears slightly contracted with the relevant  $Ti-(\mu_3-O)$  distances found to be 1.955(3)–1.958(3) Å (average 1.957 Å) and the  $Ti-(\mu-O)$  bond lengths found to be 2.102(3)–2.072(3) Å (average 2.089 Å). Additionally, the  $Ti \cdots Ti$  distances in the symmetry-related structural units  $Ti_3(\mu_3-O)$  (3.300(1)–3.292(1) Å, average 3.296 Å) are shorter than those observed in the Zr analogue (3.471(1)–3.481(1) Å, average 3.474 Å). The three angles in the symmetry-related  $Ti_3$  triangles are almost  $60^\circ$ , forming  $Ti_3$  equilateral triangles in a manner similar to that for the  $Zr_3$ -based triangles observed in 2. The metrical parameters of the structure of compound 3 (Figure 3) are very similar to those observed in 2.

At this point, it is worth noting that the ligands  $H_3$ dihybo and  $H_3$ pidiox<sup>16a</sup> (Scheme 1), which have donor atoms in three neighboring positions of the rings, gave the hexanuclear titanium compounds 1 and  $K_6[Ti_6(\mu_3-O)_2(\mu_2-O)_3(OCH_3)_6(\mu_2-Hpidiox)_4(\mu_2-pidiox)_2] \cdot 7.5CH_3OH$  (4),<sup>16a</sup> respectively, with the same core structure [ $Ti_6(\mu_3-O)_2(\mu-O)_3$ ]. This observation might demonstrate a new strategy to control the formation of hexanuclear titanium clusters.

**Solid State UV-Vis-NIR Spectroscopy.** Figure 4 shows the solid-state UV-vis-NIR spectra of compounds 1, 3, and 4.<sup>16a</sup> A comparison of the spectra of the titanium compounds 4<sup>16a</sup> and 1 (this work) reveals a 200 nm expansion of the absorbance band of 1 related to 4 toward the red region of the spectra (Figure 4). The band gaps for the three compounds were found to be 1.48, 2.34, and 2.13 eV, respectively, and were calculated from the solid state spectra by the Kubelka-Munk method.<sup>37</sup> These low band gap values for compounds 1 and 3 reveal their potential use as semiconducting photocatalysts, and thus, it is crystal clear that the marriage of the catechol moiety with the oxime group was quite successful in the modulation of the band gaps of  $TiO_2$  and  $ZrO_2$ . At this point, it is worth noting that the 1.48 eV band gap in 1 constitutes the lowest value reported thus far for any titanium oxide cluster. The synergistic effect of the oxime group presumably plays a vital role in achieving such a low value for the band gap in 1.

**NMR Spectroscopy.** Table 1 displays the  $^1H$  NMR chemical shifts of the ligand  $H_3$ dihybo and of compounds 1 and 3 in solution ( $CD_3OD$ ), and Table 2 displays the  $^{13}C$  NMR chemical shifts of  $H_3$ dihybo, 1, and 3 in solution as assigned by 2D spectra

Table 1.  $^1H$  NMR Chemical Shifts (ppm) for  $H_3$ dihybo, 1, and 3 and the Shielding/Desielding Effect ( $\Delta\delta$ , ppm) upon Complexation

	$H_3$ dihybo	1/ $\Delta\delta^*$	3/ $\Delta\delta^*$
H(7)	8.19	7.85/−0.34	7.86/−0.33
H(4)	6.80	6.78/−0.02	6.83/+0.03
H(5)	6.72	6.86/+0.16	6.74/+0.02
H(6)	6.76	6.43/−0.33	6.32/−0.41

Table 2.  $^{13}C$  NMR Chemical Shifts for  $H_3$ dihybo, 1, and 3 and the Shielding/Desielding Effect ( $\Delta\delta$ ) upon Complexation

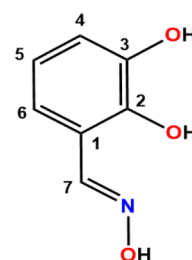
	$H_3$ dihybo	1/ $\Delta\delta^a$	3/ $\Delta\delta^a$
C(1)	117.6	114.8/−2.8	115.8/−1.8
C(2)	146.5	152.8/+6.3	154.2/+8.7
C(3)	146.4	153.6/+8.2	153.9/+7.5
C(4)	120.4	115.5/−4.9	118.6/−1.8
C(5)	118.8	121.6/+2.8	121.0/+2.2
C(6)	121.7	123.4/+1.7	123.8/+2.1
C(7)	152.3	148.1/−4.2	151.5/−0.8

$$^a\Delta\delta = \delta_{M-L} - \delta_L.$$

(( $^1H$ ,  $^{13}C$ ) HSQC/HMBC spectra, see Figures S1 and S2). The numbering of the carbon atoms of the ligand  $H_3$ dihybo is depicted in Scheme 4.

The  $^1H$  and  $^{13}C$  NMR spectra of compounds 1 and 3 in solution gave peaks shifted in comparison to the peaks of the free ligand due to the ligation of  $H_3$ dihybo<sup>2−</sup> to the Ti and Zr metal ions. In particular, C(2) and C(3) show a strong deshielding for both 1 (+6.3 and +8.2 ppm; see Table 2) and 3 (+8.7 and +7.5

Scheme 4. Numbering of the Carbon Atoms of the Ligand  $H_3$ dihybo



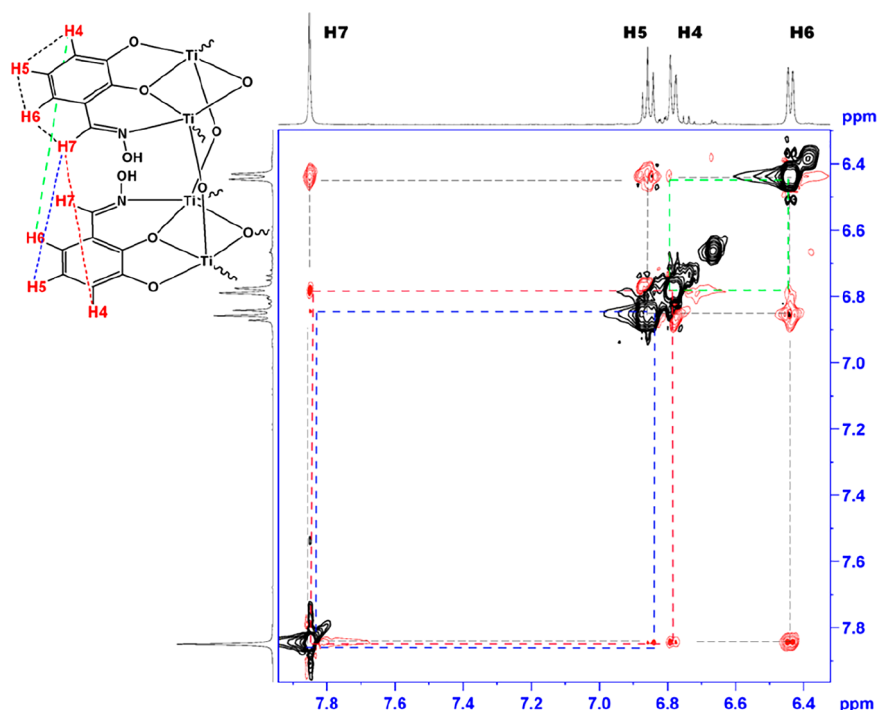


Figure 5. 2D  $\{^1\text{H}\}$  NOESY spectrum of compound 1 and the assignments of the NOESY interactions.

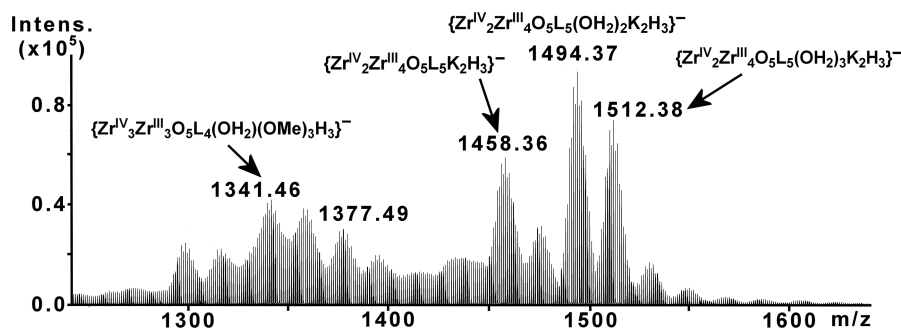


Figure 6. Negative mode electrospray ionization mass spectrum (ESI-MS) of the  $\{\text{Zr}_6\}$  (3) cluster in  $\text{CH}_3\text{OH}$ .

ppm; see Table 2) due to the ligation of the deprotonated catecholate oxygen atoms with the metal atoms. The coordination of the metal ions to the oxime nitrogen atom causes shielding of C(7) for both 1 ( $-4.2$  ppm; see Table 2) and 3 ( $-0.8$  ppm; see Table 2). The proton attached to the C(7) carbon atom is also highly deshielded for both complexes ( $\Delta\delta \approx +4.2$  ppm) presumably due to the complexation of the metal atoms with the oxime nitrogen atom and/or the formation of intramolecular hydrogen bond between the oxime proton of one ligand with the catecholate oxygen atom (C(3)–O $^-$ ) of the neighboring Hdihybo $^{2-}$ .

The differences in the C and H shielding/deshielding values between 1 and 3 might be due to the different through-space neighboring anisotropy interactions induced by the applied magnetic field on either the Ti–O and Zr–O bonds or the  $\text{Ti}_3\text{O}$  and  $\text{Zr}_3\text{O}$  metalloaromatic cores, respectively (see Tables 1 and 2).

The  $\Delta\delta$  values of H(4) protons in 1 and 3 do not follow the expected trend: that is, both are either negative or positive. A reasonable explanation for this is that these values are so small, close to zero, in marked contrast to those of all hydrogen and carbon atoms and even slight differences, such as solvent/bulk

properties of molecules around the solute of the proton, minor variance in temperature, etc., alter the “expected trend”.

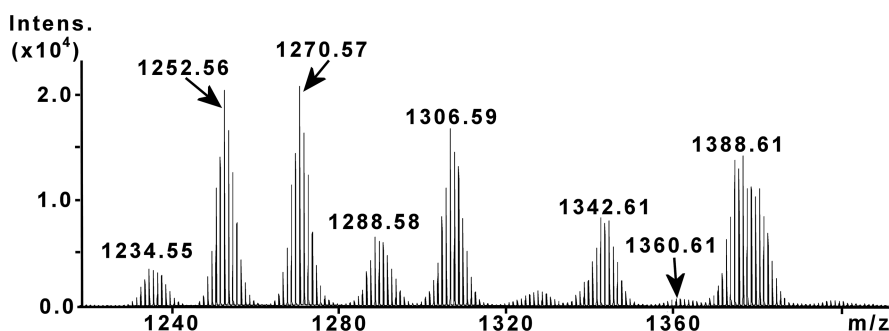
The 2D  $\{^1\text{H}\}$  NOESY-EXSY spectra of compounds 1 and 3 in solution gave strong NOESY cross peaks between the neighboring protons of the ligand (H(7)–H(6), H(6)–H(5), H(5)–H(4)) as shown in Figure 5. In addition to the intraligand proton interactions, the 2D  $\{^1\text{H}\}$  NOESY-EXSY spectra gave weaker NOESY peaks between the protons H(7)–H(4), H(7)–H(5), and H(4)–H(6) (Figure 5). These NOESY peaks were assigned to the interactions between the protons of the ligands belonging to the two  $\text{M}_3(\text{Hdihybo}^{2-})_3$  planes in the complexes, as shown for complex 1 in Figure 5. The intensity of the NOESY cross peaks suggests that the distances between the protons 4–7 are  $\text{H}(7)\text{--H}(4) < \text{H}(4)\text{--H}(6) < \text{H}(7)\text{--H}(5)$ , which are in agreement with the distances in the crystal structures of 1 and 3. Thus, compounds 1 and 3, in solution, retain their structural integrity. The NMR spectra of 1 and 3 in  $\text{D}_2\text{O}$  gave features similar to those observed in deuterated methanol, and this fact supports that 1 and 3 are hydrolytically stable.

**ESI-MS Spectrometry.** In an effort to characterize further the hexanuclear zirconium(IV) and titanium(IV) clusters in solution, we employed high-resolution ESI-MS to determine

**Table 3. Representation of the Experimentally Identified and Simulated  $m/z$  Values of Distribution Envelopes of  $\{Zr_6\}$  Cluster**

exptl	theor	charge	formula <sup>a</sup>
1716.36	1716.49	-1	$\{Zr^{IV}_2Zr^{III}_4O_5(C_7NO_3H_4)_6(OCH_3)(OH_2)_2K_3H_5\}^-$
1512.38	1512.48	-1	$\{Zr^{IV}_2Zr^{III}_4O_5(C_7NO_3H_4)_5(OH_2)_3K_2H_3\}^-$
1494.37	1494.47	-1	$\{Zr^{IV}_2Zr^{III}_4O_5(C_7NO_3H_4)_5(OH_2)_2K_2H_3\}^-$
1476.36	1476.46	-1	$\{Zr^{IV}_2Zr^{III}_4O_5(C_7NO_3H_4)_5(OH_2)K_2H_3\}^-$
1458.36	1458.45	-1	$\{Zr^{IV}_2Zr^{III}_4O_5(C_7NO_3H_4)_5K_2H_3\}^-$
1377.49	1377.59	-1	$\{Zr^{IV}_3Zr^{III}_3O_5(C_7NO_3H_4)_4(OCH_3)_3(OH_2)_3H_3\}^-$
1357.47	1357.56	-1	$\{Zr^{IV}_3Zr^{III}_3O_5(C_7NO_3H_4)_4(OCH_3)_3(OH_2)_2H\}^-$
1341.46	1341.57	-1	$\{Zr^{IV}_3Zr^{III}_3O_5(C_7NO_3H_4)_4(OCH_3)_3(OH_2)_3H\}^-$
773.75	773.85	-1	$\{Zr_3^{III}O(C_7NO_3H_4)_2(OCH_3)_3(OH_2)_5H\}^-$
755.75	755.85	-1	$\{Zr_3^{III}O(C_7NO_3H_4)_2(OCH_3)_3(OH_2)_4H\}^-$
737.74	737.84	-1	$\{Zr_3^{III}O(C_7NO_3H_4)_2(OCH_3)_3(OH_2)_3H\}^-$

<sup>a</sup>Contamination of compound 3 with small amounts of KCl during the synthesis can be easily detected by the high-resolution electrospray ionization Q-TOF instrument with a detection limit much lower than that of the elemental analysis.

**Figure 7.** Negative mode electrospray ionization mass spectrum (ESI-MS) of  $\{Ti_6\}$  (1) cluster in  $CH_3OH$ .

unambiguously the structural integrity and composition of the zirconium- and titanium-based species in solution.<sup>38</sup> The ESI-MS studies were performed in methanol. In both cases, the observation of a higher intensity set of distribution envelopes is due to the existence of the hexanuclear moiety, resulting from the combination of protons, counterions, and solvent molecules. In the case of the zirconium species 3, the region of higher  $m/z$  values is populated by a series of distribution envelopes assigned to -1 charged species and correspond to the intact  $\{Zr_6\}$  cluster (Figure 6). In this case three of the coordinating axial groups have been removed during the ionization process (e.g.,  $\{Zr^{IV}_2Zr^{III}_4O_5(C_7NO_3H_4)_6(OH_2)_2(OCH_3)_3K_3H_5\}^-$ ; Table 3). In both cases, the observation of different oxidation states for the metal centers and the presence of other fragments during the course of the studies is due to the ionization and transfer processes and has been observed in numerous occasions.<sup>39–41</sup>

Interestingly, the lower  $m/z$  region (ca. 700–800) revealed the presence of fundamental trimeric building blocks generated during the ionization process. The distribution envelopes centered at  $m/z$  773.75, 755.75, and 737.74 have been identified as the intact Zr-oxo-centered triangles associated with a different number of counterions and solvent molecules. The identification of the building blocks that appear in the mass spectrometry studies suggests the existence of an underlying sequential mechanism of assembly, where the initial formation of trimeric clusters takes place prior to their subsequent self-assembly into the hexanuclear species that finally crystallize. A similar behavior has been observed in the solution studies conducted for  $\{Ti_6\}$  species reported recently.<sup>16a</sup> More specifically, we observed the fully reduced  $\{Zr_3^{III}O(C_7NO_3H_4)_2(OCH_3)_3(OH_2)_5H\}^-$  (773.75),  $\{Zr_3^{III}O(C_7NO_3H_4)_2(OCH_3)_3(OH_2)_4H\}^-$  (755.75), and

$\{Zr_3^{III}O(C_7NO_3H_4)_2(OCH_3)_3(OH_2)_3H\}^-$  (737.74) Zr-based oxo-centered molecular triangles, respectively.

In a similar manner, investigation of the titanium adduct in solution under the same experimental conditions revealed a series of distribution envelopes with different amounts of solvent molecules associated with the intact hexanuclear cluster of the general formula  $\{Ti^{IV}_3Ti^{III}_3O_5(C_7NO_3H_4)_5(OH_2)_x\}^-$ , where  $x = 0–8$  (Figure 7 and Table 4). Smaller fragments of the cluster

**Table 4. Representation of the Experimentally Identified and Simulated  $m/z$  Values of Distribution Envelopes of  $\{Ti_6\}$  Cluster**

exptl	theor.	charge	formula
1234.55	1234.66	-1	$\{Ti^{IV}_3Ti^{III}_3O_5(C_7NO_3H_4)_5\}^-$
1252.56	1252.66	-1	$\{Ti^{IV}_3Ti^{III}_3O_5(C_7NO_3H_4)_5(OH_2)\}^-$
1270.57	1270.67	-1	$\{Ti^{IV}_3Ti^{III}_3O_5(C_7NO_3H_4)_5(OH_2)_2\}^-$
1288.58	1288.57	-1	$\{Ti^{IV}_3Ti^{III}_3O_5(C_7NO_3H_4)_5(OH_2)_3\}^-$
1306.59	1306.69	-1	$\{Ti^{IV}_3Ti^{III}_3O_5(C_7NO_3H_4)_5(OH_2)_4\}^-$
1342.61	1342.71	-1	$\{Ti^{IV}_3Ti^{III}_3O_5(C_7NO_3H_4)_5(OH_2)_6\}^-$
1360.61	1360.71	-1	$\{Ti^{IV}_3Ti^{III}_3O_5(C_7NO_3H_4)_5(OH_2)_7\}^-$
1388.61	1388.72	-1	$\{Ti^{IV}_3Ti^{III}_3O_5(C_7NO_3H_4)_5(OH_2)_8\}^-$
921.75	921.81	-1	$\{Ti^{IV}_4Ti^{III}O_5(C_7NO_3H_4)_4H_2\}^-$
939.75	939.82	-1	$\{Ti^{IV}_4Ti^{III}O_5(C_7NO_3H_4)_4H_2(OH_2)\}^-$

occurring during the studies were observed at lower  $m/z$  values, such as  $\{Ti^{IV}_4Ti^{III}O_5(C_7NO_3H_4)_4H_2\}^-$  (921.75),  $\{Ti^{IV}_4Ti^{III}O_5(C_7NO_3H_4)_4H_2(OH_2)\}^-$  (939.75), and  $\{Ti^{IV}_4Ti^{III}O_5(C_7NO_3H_4)_4H_2(OH_2)\}^-$  (939.75).

**Photocurrent Response.** The charge-separation efficiency of a semiconductor material is one of the important parameters which define its potential for practical applications. The photocurrent responses of two photoelectrodes based on

compounds **1** and **3** have been determined using a three-electrode setup. As shown in Figure 8, clear photocurrent

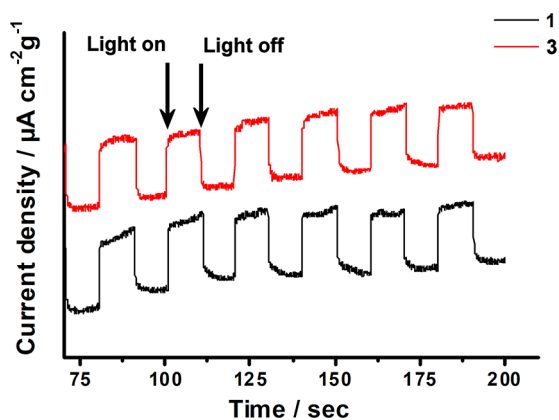


Figure 8. Photocurrent densities of compounds **1** and **3** (0.1 M Na<sub>2</sub>SO<sub>4</sub> solution).

responses were observed for both compounds. Upon illumination, the photocurrents were quickly generated without an obvious intensity decrease and remained constant during the measurement. When the light source was switched off, the photocurrents rapidly decayed, indicative of their good photoelectric response and photophysical stability during the experiment. The two compounds exhibited comparable photocurrent densities per gram of deposited material and were found to be approximately 40 mA cm<sup>-2</sup> g<sup>-1</sup>.

**Theoretical Study.** Having in mind the previously reported<sup>16a</sup> observation of the metalloaromaticity phenomenon exhibited by the hexanuclear titanium compound **4** with the ligand (2Z,6Z)-piperidine-2,6-dione dioxime (H<sub>3</sub>pidiox, <sup>16a</sup> Scheme 1), we investigated whether the cyclic trinuclear metallic ring cores M<sup>IV</sup><sub>3</sub> (M = Ti, Zr) of **1** and **2** exhibit metalloaromaticity<sup>18g</sup> as well, employing DFT electronic structure calculation methods.<sup>16a</sup> The diatropic/paratropic ring current signals are associated with the aromaticity/antiaromaticity of the metallic ring cores. In this context, the nucleus independent chemical shift (NICS), by computation of the respective NICS<sub>zz</sub> scan curves, could be used very effectively as good indicators of aromaticity/antiaromaticity of cyclic metallic ring cores.<sup>20b,21,42</sup>

Accordingly, we calculated the NICS<sub>zz</sub> scan curve of the cyclo-M<sub>3</sub> trinuclear metallic cores (M = Ti or Zr) with the GIAO (gauge-including atomic orbitals) DFT method<sup>26,27</sup> as implemented in the Gaussian09 series of programs<sup>28</sup> employing the PBE0 functional in combination with the 6-31G(d,p) and the Def2-TZVP basis sets for the nonmetal and the Ti and Zr metal atoms, respectively. The computational protocol will henceforth be denoted as GIAO/PBE0/Def2-TZVP(M)U6-31G(d,p)(E). The NICS<sub>zz</sub> curves were calculated for the model systems [M<sup>IV</sup><sub>3</sub>(μ<sub>3</sub>-O)(μ-Hdihybo)<sub>3</sub>](OCH<sub>3</sub>)<sub>3</sub>(OH)<sub>3</sub> (M = Ti (**1M**), Zr (**2M**)), where the coordination environments of **1** and **2** were truncated by the use of methoxy and hydroxyl groups in order to reduce the computational cost. In addition, we have calculated the NICS<sub>zz</sub> curves for the simpler model [M<sup>IV</sup><sub>3</sub>(μ-Hdihybo)<sub>3</sub>] (M = Ti (**3M**), Zr (**4M**)) complexes in order to study the effect of the μ<sub>3</sub>-O ligand on the aromaticity/antiaromaticity of the trimetallic ring cores. The NICS<sub>zz</sub> scan curves were obtained by placing Bq ghost atoms on a line, coinciding with the z axis, being vertical to the trimetallic ring core and passing through the

ring center (Figure 9). The molecular structures of the model compounds used in this study along with the positions of the Bq ghost atoms are depicted in Figure 9.

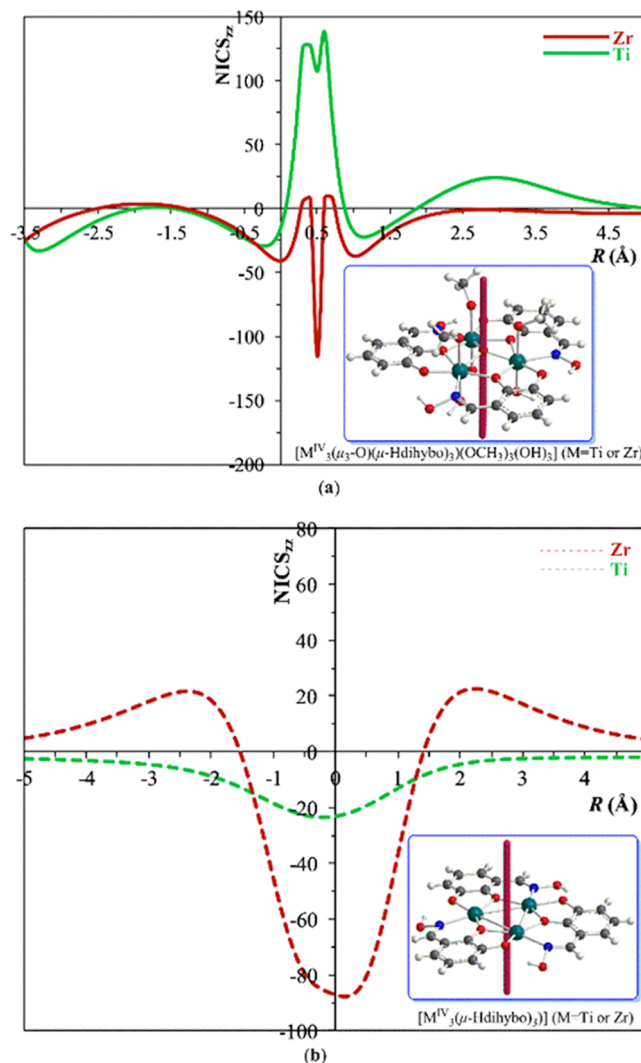
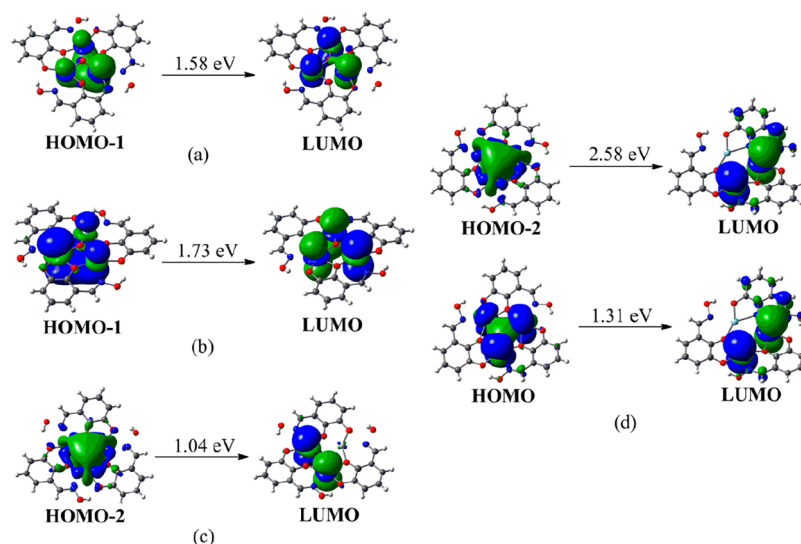


Figure 9. NICS<sub>zz</sub> scan profiles of **1M** ([Ti<sup>IV</sup><sub>3</sub>(μ<sub>3</sub>-O)(μ-Hdihybo)<sub>3</sub>(OCH<sub>3</sub>)<sub>3</sub>(OH)<sub>3</sub>]) and **2M** ([Zr<sup>IV</sup><sub>3</sub>(μ<sub>3</sub>-O)(μ-Hdihybo)<sub>3</sub>(OCH<sub>3</sub>)<sub>3</sub>(OH)<sub>3</sub>]) (a) and **3M** ([Ti<sup>IV</sup><sub>3</sub>(μ-Hdihybo)<sub>3</sub>]) and **4M** ([Zr<sup>IV</sup><sub>3</sub>(μ-Hdihybo)<sub>3</sub>]) (b) calculated at the PBE0/6-31G(d,p) level (red lines for **1M/3M**, green lines for **2M/4M**).

Figure 9a shows the calculated NICS<sub>zz</sub> scan curves for the model compounds bearing the μ<sub>3</sub>-O ligand, **1M** and **2M** (solid green and red lines, respectively). The NICS<sub>zz</sub> scan curves for the model compounds without the μ<sub>3</sub>-O ligand, **3M** and **4M** (dashed green and red lines, respectively) are depicted in Figure 9b.

Let us first examine the model systems bearing the μ<sub>3</sub>-O ligand which is capping the M<sub>3</sub> ring. Inspection of Figure 9a (solid green line) reveals that the NICS<sub>zz</sub> curve of **1M** exhibits a NICS<sub>zz</sub>(0) value equal to -14.5 ppm while the NICS<sub>zz</sub>(1) value amounts to -18.4 ppm. Both values indicate that the cyclo-Ti<sub>3</sub> metallic ring core is aromatic. The NICS<sub>zz</sub> scan curves exhibiting two maxima at a certain distance above and below the molecular plane defined by the three metal atoms and the three Hdihybo<sup>2-</sup> ligands are typical for σ + π aromatics where the π-diatropic ring current overwhelms the σ-type current.<sup>43</sup>



**Figure 10.** 3D plots of the molecular orbitals and significant  $T_{xy}$ -allowed transitions leading to the diamagnetic ring currents in (a) **1M**, (b) **2M**, (c) **3M**, and (d) **4M**.

The  $NICS_{zz}$  curve of **2M**, depicted in Figure 9a (solid red line), follows the pattern of the respective  $NICS_{zz}$  curves calculated for the Ti system (Figure 9a, solid green line). Along these lines the  $NICS_{zz}(0)$  value is equal to  $-40.1$  ppm and the  $NICS_{zz}(1)$  value amounts to  $-37.3$  ppm, while the  $NICS_{zz}(-1)$  value is only  $-5.2$  ppm. For the Zr model system we again observe three aromaticity zones ranging from strongly aromatic to slightly aromatic in a manner similar to that of its Ti counterpart model system. It is worth noting that the aromaticities of these model systems are comparable to that reported for a similar system<sup>16a</sup> bearing a *cyclo*-Ti<sub>3</sub> trinuclear ring core with an  $NICS_{zz}(1)$  value of  $-23.2$  ppm. Obviously, the magnitude of aromaticity of the *cyclo*-M<sub>3</sub> trinuclear ring cores depends on the nature of the metal centers as well as of the surrounding ligands.

In order to further delineate the obscured aromaticity of the metallic ring cores of these systems, we have also calculated the  $NICS_{zz}$  curves for the even simpler model systems, namely  $[M^{IV}_3(\mu\text{-HdiHybo})_3]$  ( $M = \text{Ti}$  (**3M**),  $\text{Zr}$  (**4M**)). In these systems we have removed the  $\mu_3\text{-O}$  capping ligands as well as the methoxy and hydroxy ligands, protruding out of the metallic ring core. Figure 9b reveals that indeed the trimetallic ring cores in both **3M** and **4M** are expected to be aromatic, with the phenomenon being more pronounced for  $M = \text{Zr}$ . The  $NICS_{zz}(0)$ ,  $NICS_{zz}(1)$ , and  $NICS_{zz}(-1)$  values are  $-23.5$ ,  $-13.0$ , and  $-18.6$  ppm, respectively, for **3M** and  $-87.2$ ,  $-36.4$ , and  $-45.7$  ppm, respectively, for **4M**. The much higher aromatic character of the Zr metallic ring can be attributed probably to the stronger overlap of the more diffuse 4d orbitals of Zr in comparison to the 3d orbitals of Ti forming the delocalized d orbital aromatic system on the respective metallic ring cores.

Upon removal of the  $\mu_3\text{-O}$  ligand and the methoxy and hydroxy ligands a dramatic changes in the  $NICS_{zz}$  curves (Figure 9b) of the trimetallic cores of **3M** and **4M** are observed. More specifically, for **3M** and **4M** the  $NICS_{zz}$  curves exhibit only one broad maximum with their shape being indicative of  $\sigma$  aromaticity.<sup>43</sup>

Figure 10 shows 3D plots of the highest occupied molecular orbitals (HOMOs) and the lowest unoccupied molecular orbitals (LUMOs) along with the lowest  $T_{xy}$ -allowed transitions calculated for **3M** and **4M**. The  $\sigma$  aromaticity of the metallic ring

cores is further corroborated by examining the shapes of the MOs involved in the  $T_{xy}$ -allowed transitions that contribute to the diamagnetic ring current (Figure 10). For **3M** the  $T_{xy}$ -allowed transition arises from a HOMO-2  $\rightarrow$  LUMO transition where the HOMO-2 is a delocalized  $\sigma$  bonding MO, constructed mainly from Ti 3d AOs (Figure 10c). For **4M** there are two  $T_{xy}$ -allowed transitions i.e., HOMO-2  $\rightarrow$  LUMO and HOMO  $\rightarrow$  LUMO, where both HOMO-2 and HOMO are  $\sigma$  delocalized bonding MOs, constructed mainly from Zr 4d AOs (Figure 10d).

For **1M**, there is only one  $T_{xy}$ -allowed transition inducing a diamagnetic ring current involving HOMO-1 and LUMO (Figure 10a). The former is a  $\pi$ -type bonding MO, while the latter is an antibonding MO, both constructed mainly from the in-phase linear combination of  $d_{z^2}$  AOs of the three Ti metal centers. The HOMO-1  $\rightarrow$  LUMO transition corresponds to relatively small excitation energy.

The shape of the  $NICS_{zz}$  curve of **2M** (Figure 9a, solid red line) is only qualitatively like that found for **1M**.

In contrast to **1M**, the  $NICS_{zz}(1)$  and  $NICS_{zz}(-1)$  values of **2M** differ significantly, being  $-3$  and  $-42$  ppm, respectively. Obviously, the  $\mu_3\text{-O}$  ligand capping the *cyclo*-Zr<sub>3</sub> ring significantly suppresses the  $NICS(1)$  value in comparison to **1M**. Note, however, that the  $NICS(0)$  value calculated for **1M** and **2M** amount to  $-38$  and  $-32$  ppm, respectively, both signifying aromaticity. Both, the  $NICS_{zz}$  scan curve shapes and the  $T_{xy}$ -allowed transition inducing  $\sigma$  diamagnetic ring current involving the HOMO-1 and LUMO (Figure 10b) point to a  $\sigma + \pi$  aromatic system, where the  $\pi$ -diatropic ring current overwhelms the  $\sigma$ -type current. Note that the Zr system exhibits enhanced aromaticity in comparison to its Ti homologue system. From the results discussed so far, it can be concluded that the aromaticity of a metallic ring core depends upon the nature of its metallic center. Moreover, we wish to point out that this is the very first example of a Zr<sub>3</sub> triangle which exhibits metalloaromaticity.

## CONCLUSIONS

In conclusion, a series of hexanuclear titanium(IV) and zirconium(IV) compounds were synthesized by a simple three-component reaction, at room temperature. The three

compounds have the same core structure  $[M^{IV}_6(\mu_3-O)_2(\mu-O)_3]$  ( $M = Ti, Zr$ ), which constitutes a unique example with a trigonal-prismatic arrangement of the six zirconium(IV) atoms and a unique  $Zr^{IV}_6$  structural motif.

The trend observed in the formation of  $[M^{IV}_6(\mu_3-O)_2(\mu-O)_3]$  ( $M = Ti, Zr$ ) structural motifs with organic molecules having donor atoms in three neighboring positions of the ligand's ring (ref 16a and this work) might reveal a new design principle to control the formation of titanium and zirconium hexanuclear clusters.

Multinuclear solution NMR showed that these hexanuclear compounds retain their integrity in both methanol and water solvents, and thus, their hydrolytic stability makes them potential building blocks for the preparation of titanium(IV) and zirconium(IV) metal organic frameworks (MOFs).

The nucleus-independent chemical shift (NICS) magnetic criterion was used in this study and revealed the aromaticity of the  $M^{IV}_3$  ( $M = Ti, Zr$ ) rings. ESI-MS measurements also support the initial formation of the  $M_3$  structural units prior to their self-assembly into the hexanuclear  $M_6$  species. The metalloaromaticity of the  $M_3$  rings and the ESI-MS measurements suggest that the  $M_3$  rings' formation play an important role in the synthesis of these hexanuclear clusters.

The successful marriage of the catechol moiety with the oxime group in the ligand  $H_3$ diHybo led to a substantial band gap reduction of the hexanuclear clusters in comparison to  $TiO_2$  and  $ZrO_2$  and induced photocurrent responses in 1 and 3. The present study opens up new avenues for the rational design of titanium- and zirconium-based clusters absorbing in the NIR region of the spectrum for numerous applications.

## ■ ASSOCIATED CONTENT

### SI Supporting Information

The Supporting Information is available free of charge at <https://pubs.acs.org/doi/10.1021/acs.inorgchem.0c02959>.

UV–vis-NIR, FT-IR, and NMR spectra and final unit cell data (PDF)

## Accession Codes

CCDC 2013476–2013478 contain the supplementary crystallographic data for this paper. These data can be obtained free of charge via [www.ccdc.cam.ac.uk/data\\_request/cif](http://www.ccdc.cam.ac.uk/data_request/cif), or by emailing [data\\_request@ccdc.cam.ac.uk](mailto:data_request@ccdc.cam.ac.uk), or by contacting The Cambridge Crystallographic Data Centre, 12 Union Road, Cambridge CB2 1EZ, UK; fax: +44 1223 336033.

## ■ AUTHOR INFORMATION

### Corresponding Authors

**Athanassios C. Tsipis** – Section of Inorganic and Analytical Chemistry and, University of Ioannina, Ioannina 45110, Greece; [orcid.org/0000-0002-0425-2235](https://orcid.org/0000-0002-0425-2235); Email: [attsipis@uoi.gr](mailto:attsipis@uoi.gr)

**Anastasios D. Keramidis** – Department of Chemistry, University of Cyprus, Nicosia 1678, Cyprus; [orcid.org/0000-0002-0446-8220](https://orcid.org/0000-0002-0446-8220); Email: [akeramid@ucy.ac.cy](mailto:akeramid@ucy.ac.cy)

**Haralampos N. Miras** – West CHEM, School of Chemistry, University of Glasgow, Glasgow G12 8QQ, U.K.; [orcid.org/0000-0002-0086-5173](https://orcid.org/0000-0002-0086-5173); Email: [charalampos.moiras@glasgow.ac.uk](mailto:charalampos.moiras@glasgow.ac.uk)

**Themistoklis A. Kabanos** – Section of Inorganic and Analytical Chemistry and, University of Ioannina, Ioannina 45110, Greece; [orcid.org/0000-0001-6944-5153](https://orcid.org/0000-0001-6944-5153); Email: [tkampano@uoi.gr](mailto:tkampano@uoi.gr)

## Authors

**Stamatis S. Passadis** – Section of Inorganic and Analytical Chemistry and, University of Ioannina, Ioannina 45110, Greece

**Michael G. Papanikolaou** – Section of Inorganic and Analytical Chemistry and, University of Ioannina, Ioannina 45110, Greece

**Alexander Elliott** – West CHEM, School of Chemistry, University of Glasgow, Glasgow G12 8QQ, U.K.

**Constantinos G. Tsiafoulis** – NMR Center, University of Ioannina, Ioannina 45110, Greece; [orcid.org/0000-0002-8254-0187](https://orcid.org/0000-0002-8254-0187)

Complete contact information is available at:

<https://pubs.acs.org/10.1021/acs.inorgchem.0c02959>

## Notes

The authors declare no competing financial interest.

## ■ ACKNOWLEDGMENTS

The research work was supported by the Hellenic Foundation for Research and Innovation (HFRI) under an HFRI Ph.D. Fellowship grant (Fellowship Number 1553) and funded by the European Regional Development Fund and the Republic of Cyprus through the Research and Innovation Foundation (Project: EXCELLENCE/1216/0515). H.N.M. thanks the University of Glasgow for supporting this work and Prof. L. Cronin for providing access to the X-ray and ESI-MS facilities.

## ■ REFERENCES

- (1) (a) Fang, W. H.; Zhang, L.; Zhang, J. A 3.6 nm  $Ti_{52}$ -Oxo Nanocluster with Precise Atomic Structure. *J. Am. Chem. Soc.* **2016**, *138*, 7480–7483. (b) Gao, M. Y.; Wang, F.; Gu, Z. G.; Zhang, D. X.; Zhang, L.; Zhang, J. Fullerene-Like Polyoxotitanium Cage with High Solution Stability. *J. Am. Chem. Soc.* **2016**, *138*, 2556–2559. (c) Zhang, G.; Liu, C.; Long, D. L.; Cronin, L.; Tung, C. H.; Wang, Y. Water-Soluble Pentagonal-Prismatic Titanium-Oxo Clusters. *J. Am. Chem. Soc.* **2016**, *138*, 11097–11100. (d) Czakler, M.; Artner, C.; Schubert, U. Two new hexanuclear titanium oxo cluster types and their structural connection to known clusters. *New J. Chem.* **2018**, *42*, 12098–12103. (e) Chen, S.; Fang, W. H.; Zhang, L.; Zhang, J. Synthesis, Structures, and Photocurrent Responses of Polyoxo-Titanium Clusters with Oxime Ligands: From  $Ti_4$  to  $Ti_{18}$ . *Inorg. Chem.* **2018**, *57*, 8850–8856. (f) Hou, J. L.; Huo, P.; Tang, Z. Z.; Cui, L. N.; Zhu, Q. Y.; Dai, J. A Titanium Oxo Cluster Model Study of Synergistic Effect of Cooordinated Dye Ligands on Photocurrent Responses. *Inorg. Chem.* **2018**, *57*, 7420–7427. (g) Zou, D. H.; Cui, L. N.; Liu, P. Y.; Yang, S.; Zhu, Q. Y.; Dai, J. Molecular Model of Dye Sensitized Titanium Oxides Based on Arylamine Dye Anchored Titanium Oxo Clusters. *Inorg. Chem.* **2019**, *58*, 9246–9252. (h) Yu, Y. Z.; Yan-Ru Zhang, Y. R.; Geng, C. H.; Sun, L.; Guo, Y.; Feng, Y. R.; Wang, Y. X.; Zhang, X. M. Precise and Wide-Ranged Band-Gap Tuning of  $Ti_6$ -Core-Based Titanium Oxo Clusters by the Type and Number of Chromophore Ligands. *Inorg. Chem.* **2019**, *58*, 16785–16791. (i) Fang, W.; H.; Zhang, L.; Zhang, J. Synthetic strategies, diverse structures and tuneable properties of polyoxo-titanium clusters. *Chem. Soc. Rev.* **2018**, *47*, 404–421. (j) Liu, X.-X.; Chen, S.; Fang, W.-H.; Zhang, L.; Zhang, J. Amino-Polyalcohol-Solvothermal Synthesis of Titanium-Oxo Clusters: From  $Ti_6$  to  $Ti_{19}$  with Structural Diversity. *Inorg. Chem.* **2019**, *58*, 7267–7273. (k) Zheng, H.; Deng, Y. K.; Ye, M. Y.; Xu, Q. F.; Kong, X. J.; Long, L. S.; Zheng, L. S. Lanthanide-Titanium Oxo Clusters as the Luminescence Sensor for Nitrobenzene Detection. *Inorg. Chem.* **2020**, *59*, 12404–12409. (2) (a) Gao, M. Y.; Chen, S.; Hu, L. X.; Zhang, L.; Zhang, J. Synthesis and photocatalytic  $H_2$  evolution properties of four titanium-oxo-clusters based on a cyclohex-3-ene-1-carboxylate ligand. *Dalton Trans.* **2017**, *46*, 10630–10634. (b) Fan, X.; Wang, J. H.; Wu, K. F.; Zhang, L.

- Zhang, J. Isomerism in Titanium-oxo Clusters: Molecular Anatase Model with Atomic Structure and Improved Photocatalytic Activity. *Angew. Chem., Int. Ed.* **2019**, *58*, 1320–1323. (c) Wang, C.; Liu, C.; Li, L. J.; Sun, Z. M. Synthesis, Crystal Structures, and Photochemical Properties of a Family of Heterometallic Titanium Oxo Clusters. *Inorg. Chem.* **2019**, *58*, 6312–6319. (d) Wang, X.; Yu, Y.; Wang, Z.; Zheng, J.; Bi, Y.; Zheng, Z. Thiocalix[4]arene-Protected Titanium–Oxo Clusters: Influence of Ligand Conformation and Ti–S Coordination on the Visible-Light Photocatalytic Hydrogen Production. *Inorg. Chem.* **2020**, *59*, 7150–7157.
- (3) (a) Su, H. C.; Wu, Y. Y.; Hou, J. L.; Zhang, G. L.; Zhu, Q. Y.; Dai, J. Dye molecule bonded titanium alkoxide: a possible new type of dye for sensitized solar cells. *Chem. Commun.* **2016**, *52*, 4072–4075. (b) Hou, J.-L.; Huo, P.; Tang, Z.-Z.; Cui, L.-N.; Zhu, Q.-Y.; Dai, J. A Titanium Oxo Cluster Model Study of Synergistic Effect of Cooordinated Dye Ligands on Photocurrent Responses. *Inorg. Chem.* **2018**, *57*, 7420–7427. (c) Zou, D.-H.; Cui, L.-N.; Liu, P.-Y.; Yang, S.; Zhu, Q.-Y.; Dai, J. Molecular Model of Dye Sensitized Titanium Oxides Based on Aryl-Amine Dye Anchored Titanium Oxo Clusters. *Inorg. Chem.* **2019**, *58* (14), 9246–9252.
- (4) Wang, S. B.; Wang, X. C. Multifunctional Metal–Organic Frameworks for Photocatalysis. *Small* **2015**, *11*, 3097–3112.
- (5) Li, N.; Liu, J.; Liu, J. J.; Dong, L. Z.; Li, S. L.; Dong, B. X.; Kan, Y. H.; Lan, Y. Q. Self-Assembly of a Phosphate-Centered PolyoxoTitanium Cluster: Discovery of the Heteroatom Keggin Family. *Angew. Chem., Int. Ed.* **2019**, *58*, 17260–17264.
- (6) (a) Brennan, B. J.; Chen, J.; Rudshiteyn, B.; Chaudhuri, S.; Mercado, B. Q.; Batista, V. S.; Crabtree, R. H.; Brudvig, G. W. Molecular Titanium-Hydroxamate Complexes as Models for TiO<sub>2</sub> Surface Binding. *Chem. Commun.* **2016**, *52*, 2972–2975. (b) Troiano, J. L.; Hu, G.; Crabtree, R. H.; Brudvig, G. W. Diazo coupling for surface attachment of small molecules to TiO<sub>2</sub> nanoparticles. *Chem. Commun.* **2020**, *56*, 9340–9343.
- (7) (a) Xu, X.; Ransom, C.; Efstathiou, P.; Irvine, J. T. A red metallic oxide photocatalyst. *Nat. Mater.* **2012**, *11*, 595–598. (b) Wang, C.; Liu, C.; Tian, H. R.; Li, L. J.; Sun, Z. M. Designed Cluster Assembly of Multidimensional Titanium Coordination Polymers: Syntheses, Crystal Structure and Properties. *Chem. - Eur. J.* **2018**, *24*, 2952–2961.
- (8) (a) Lv, H. T.; Li, H. M.; Zou, G. D.; Cui, Y.; Huang, Y.; Fan, Y. Titanium-oxo clusters functionalized with catecholate-type ligands: modulating the optical properties through charge transfer transitions. *Dalton Trans.* **2018**, *47*, 8158–8163. (b) Yu, Y.-Z.; Zhang, Y.-R.; Geng, C.-H.; Sun, L.; Guo, Y.; Feng, Y.-R.; Wang, Y.-X.; Zhang, X.-M. Precise and Wide-Ranged Band-Gap Tuning of Ti<sub>6</sub>-Core-Based Titanium Oxo Clusters by the Type and Number of Chromophore Ligands. *Inorg. Chem.* **2019**, *58*, 16785–16791.
- (9) Hoffmann, M. R.; Martin, S. T.; Choi, W. Y.; Bahnemann, D. W. Environmental Applications of Semiconductor Photocatalysis. *Chem. Rev.* **1995**, *95*, 69–96.
- (10) Lai, Y.-S.; Su, Y. H.; Lin, M. I. Photochemical water splitting performance of fluorescein, rhodamine B, and chlorophyll-Cu supported on ZrO<sub>2</sub> nanoparticles layer anode. *Dyes Pigm.* **2014**, *103*, 76–81.
- (11) Ksapabutr, B.; Chalermkiti, T.; Wongkasemjit, S.; Panapoy, M. Fabrication of scandium stabilized zirconia thin film by electrostatic spray deposition technique for solid oxide fuel cell electrolyte. *Thin Solid Films* **2010**, *518*, 6518–6521.
- (12) (a) Zhao, Y.; Zhang, Y.; Li, J.; Du, X. Solvothermal synthesis of visible-light-active N-modified ZrO<sub>2</sub> nanoparticles. *Mater. Lett.* **2014**, *130*, 139–142. (b) Jiang, W.; He, J.; Zhong, J.; Lu, J.; Yuan, S.; Liang, B. Preparation, and photocatalytic performance of ZrO<sub>2</sub> nanotubes fabricated with anodization process. *Appl. Surf. Sci.* **2014**, *307*, 407–413. (c) Ismael, M.; Wu, Y.; Wark, M. Photocatalytic activity of ZrO<sub>2</sub> composites with graphitic carbon nitride for hydrogen production under visible light. *New J. Chem.* **2019**, *43*, 4455–4462.
- (13) Botta, S. G.; Navio, J. A.; Hidalgo, M. C.; Restrepo, G. M.; Litter, M. I. Photocatalytic properties of ZrO<sub>2</sub> and Fe/ZrO<sub>2</sub> semiconductors prepared by a sol–gel technique. *J. Photochem. Photobiol., A* **1999**, *129*, 89–99 and references therein.
- (14) (a) Bai, Y.; Dou, Y.; Xie, L.-H.; Rutledge, W.; Li, J.-R.; Zhou, H.-C. Zr-based metal–organic frameworks: design, synthesis, structure, and applications. *Chem. Soc. Rev.* **2016**, *45*, 2327–2367 and references therein. (b) Yang, D.; Gaggioli, C.-A.; Ray, D.; Babucci, M.; Gagliardi, L.; Gatesa, B. C. Tuning Catalytic Sites on Zr<sub>6</sub>O<sub>8</sub> Metal Organic Framework Nodes via Ligand and Defect Chemistry probed with t-Butyl Alcohol Dehydration to Isobutylene. *J. Am. Chem. Soc.* **2020**, *142* (17), 8044–8056. (c) Diao, Y.; Hu, J.; Cheng, S.; Ma, F.; Li, M.-Q.; Hu, X.; Li, Y.-Y.; He, J.; Xu, Z. Dense Alkyne Arrays of a Zr(IV) Metal–Organic Framework Absorb CO<sub>2</sub>(CO)<sub>8</sub> for Functionalization. *Inorg. Chem.* **2020**, *59*, 5626–5631. (d) Wang, H.; Yu, L.; Lin, Y.; Peng, J.; Teat, S. J.; Williams, L. J.; Li, J. Adsorption of Fluorocarbons and Chlorocarbons by Highly Porous and Robust Fluorinated Zirconium Metal–Organic Frameworks. *Inorg. Chem.* **2020**, *59*, 4167–4171. (e) Taddei, M.; van Bokhoven, J. A.; Ranocchiari, M. Influence of Water in the Synthesis of the Zirconium-Based Metal–Organic Framework UiO-66: Isolation and Reactivity of [ZrCl(OH)<sub>2</sub>(DMF)<sub>2</sub>]-Cl. *Inorg. Chem.* **2020**, *59* (11), 7860–7868.
- (15) (a) Assi, H.; Haouas, M.; Mouchaham, G.; Martineau-Corcoss, C.; Allain, C.; Clavier, G.; Guillou, N.; Serre, C.; Devic, T. MgTi(cat)<sub>3</sub>, a promising precursor for the preparation of Ti–MOFs? *Polyhedron* **2018**, *156*, 111–115. (b) Cooper, S. R.; Koh, Y. B.; Raymond, K. N. Synthetic, Structural, and Physical Studies of Bis(triethylammonium) Tris(catecholato)vanadate(IV), Potassium Bis(catecholato)-oxovanadate(IV), and Potassium Tris(catecholato)vanadate(III). *J. Am. Chem. Soc.* **1982**, *104*, 5092–5102. (c) Harris, W. R.; Carrano, C. J.; Cooper, S. R.; Sofen, S. R.; Avdeef, A. E.; McArdle, J. V.; Raymond, K. N. Coordination Chemistry of Microbial Iron Transport Compounds. 19. Stability Constants and Electrochemical Behavior of Ferric Enterobactin and Model Complexes. *J. Am. Chem. Soc.* **1979**, *101*, 6097. (d) Sofen, S. R.; Cooper, S. R.; Raymond, K. N. Crystal and Molecular Structures of Tetrakis(catecholato)hafnate(IV) and -cerate(IV). Further Evidence for a Ligand Field Effect in the Structure of Tetrakis(catecholato)uranate(IV). *Inorg. Chem.* **1979**, *18*, 1611–1616. (e) Borgias, B. A.; Cooper, S. R.; Koh, Y. B.; Raymond, K. N. Synthetic, Structural, and Physical Studies of Titanium Complexes of Catechol and 3,5-Di-tert-butylcatechol. *Inorg. Chem.* **1984**, *23*, 1009–1016.
- (16) (a) Passadis, S. S.; Hadjithoma, S.; Kalampounias, A. G.; Tsipis, A. C.; Sproules, S.; Miras, H. N.; Keramidias, A. D.; Kabanos, T. A. Synthesis, structural and physicochemical characterization of a new type Ti<sub>6</sub>-oxo cluster protected by a cyclic imide dioxime ligand. *Dalton Trans.* **2019**, *48*, 5551–5559. (b) Baumann, S. O.; Bendova, M.; Puchberger, M.; Schubert, U. Modification of Titanium Isopropoxide with Aromatic Aldoximes. *Eur. J. Inorg. Chem.* **2011**, *2011*, 573–580. (c) Baumann, S. O.; Puchberger, M.; Schubert, U. Oximate-substituted zirconium alkoxides. *Dalton Trans.* **2011**, *40*, 1401–1406.
- (17) (a) Wood, P. A.; Forgan, R. S.; Parsons, S.; Pidcock, E.; Tasker, P. A. 3-Hydroxysalicylaldehyde. *Acta Crystallogr.* **2007**, *E63*, o3131. (b) Tarai, A.; Baruah, J. B. A study on fluoride detection and assembly of hydroxyaromatic aldoximes caused by tetraethylammonium fluoride. *CrystEngComm* **2015**, *17*, 2301–2309. (c) Song, J.; Zhao, H.; Liu, Y.; Han, H.; Li, Z.; Chu, W.; Sun, Z. Efficient symmetrical bidentate dioxime ligand accelerated homogeneous palladium-catalyzed Suzuki–Miyaura coupling reactions of aryl chlorides. *New J. Chem.* **2017**, *41*, 372–376.
- (18) (a) Islas, R.; Poater, J.; Matito, E.; Solà, M. Molecular structures of M<sub>2</sub>N<sub>2</sub><sup>2-</sup> (M and N = B, Al, and Ga) clusters using the gradient embedded genetic algorithm. *Phys. Chem. Chem. Phys.* **2012**, *14*, 14850–14859. (b) Poater, J.; Feixas, F.; Bickelhaupt, F. M.; Solà, M. All-metal aromatic clusters M<sub>4</sub><sup>2-</sup> (M = B, Al, and Ga). Are p-electrons distortive or not? *Phys. Chem. Chem. Phys.* **2011**, *13*, 20673–20681. (c) Boldyrev, A. I.; Wang, L. S. All-Metal Aromaticity and Antiaromaticity. *Chem. Rev.* **2005**, *105*, 3716–3757. (d) Tsipis, C. A. DFT Study of “All-Metal” Aromatic Compounds. *Coord. Chem. Rev.* **2005**, *249*, 2740–2762. (e) Zubarev, D. Y.; Averkiev, B. B.; Zhai, H.-J.; Wang, L.-S.; Boldyrev, A. I. Aromaticity and Antiaromaticity in Transition-Metal Systems. *Phys. Chem. Chem. Phys.* **2008**, *10*, 257–267. (f) Li, L.-J.; Ali, B.; Chen, Z.; Sun, Z.-M. Recent Advances in Aromatic Antimony Clusters. *Chin. J. Chem.* **2018**, *36*, 955–960. (g) Tsipis, C. A.

DFT challenge of intermetallic interactions: From metallophilicity and metalloaromaticity to sextuple bonding. *Coord. Chem. Rev.* **2017**, *345*, 229–262.

(19) (a) Shetty, S.; Kar, R.; Kanhere, D. G.; Pal, S. Intercluster Reactivity of Metalloaromatic and Antiaromatic Compounds and Their Applications in Molecular Electronics: A Theoretical Investigation. *J. Phys. Chem. A* **2006**, *110*, 252–256. (b) Li, X.; Sun, J.; Zeng, Y.; Sun, Z.; Zheng, S.; Meng, L. Nature of Chemical Bonding and Metalloaromaticity of  $\text{Na}_2[(\text{M}\text{Arx}')_3]$  ( $\text{M} = \text{B}, \text{Al}, \text{Ga}$ ;  $\text{Arx}' = \text{C}_6\text{H}_5\text{-}2,6\text{-}(\text{C}_6\text{H}_5)_2$ ). *J. Phys. Chem. A* **2012**, *116*, 5491–5496. (c) Nembach, E. Order strengthening: recent developments, with special reference to aluminium–lithium-alloys. *Prog. Mater. Sci.* **2000**, *45*, 275–338.

(20) (a) Schleyer, P. v. R.; Maerker, C.; Dransfeld, A.; Jiao, H. J.; van Eikema Hommes, N. J. R. Nucleus-independent chemical shifts: a simple and efficient aromaticity probe. *J. Am. Chem. Soc.* **1996**, *118*, 6317–6318. (b) Chen, Z.; Wannere, C. S.; Corminboeuf, C.; Puchta, R.; Schleyer, P. v. R. Nucleus-Independent Chemical Shifts (NICS) as an Aromaticity Criterion. *Chem. Rev.* **2005**, *105*, 3842–3888.

(21) Schleyer, P. v. R.; Maerker, C.; Dransfeld, A.; Jiao, H.; van Eikema Hommes, N. J. R. Nucleus-Independent Chemical Shifts: A Simple and Efficient Aromaticity Probe. *J. Am. Chem. Soc.* **1996**, *118*, 6317–6318.

(22) Sheldrick, G. M. Phase Annealing in SHELX-90: Direct Methods for Larger Structures. *Acta Crystallogr., Sect. A: Found. Crystallogr.* **1990**, *46*, 467.

(23) Sheldrick, G. M. A short history of SHELX. *Acta Crystallogr., Sect. A: Found. Crystallogr.* **2008**, *64*, 112.

(24) Farrugia, L. J. WinGX Program Features. *J. Appl. Crystallogr.* **1999**, *32*, 837.

(25) Clark, R. C.; Reid, J. S. The Analytical Calculation of Absorption in Multifaceted Crystals. *Acta Crystallogr., Sect. A: Found. Crystallogr.* **1995**, *51*, 887.

(26) Ditchfield, R. Self-consistent perturbation theory of diamagnetism. *Mol. Phys.* **1974**, *27*, 789–807.

(27) Gauss, J. Effects of electron correlation in the calculation of nuclear magnetic resonance chemical shifts. *J. Chem. Phys.* **1993**, *99*, 3629–3643.

(28) Frisch, M. J.; Trucks, G. W.; Schlegel, H. B.; Scuseria, G. E.; Robb, M. A.; Cheeseman, J. R.; Scalmani, G.; Barone, V.; Mennucci, B.; Petersson, G. A.; Nakatsuji, H.; Caricato, M.; Li, X.; Hratchian, H. P.; Izmaylov, A. F.; Bloino, J.; Zheng, G.; Sonnenberg, J. L.; Hada, M.; Ehara, M.; Toyota, K.; Fukuda, R.; Hasegawa, J.; Ishida, M.; Nakajima, T.; Honda, Y.; Kitao, O.; Nakai, H.; Vreven, T.; Montgomery, J. A., Jr.; Peralta, J. E.; Ogliaro, F.; Bearpark, M.; Heyd, J. J.; Brothers, E.; Kudin, K. N.; Staroverov, V. N.; Kobayashi, R.; Normand, J.; Raghavachari, K.; Rendell, A.; Burant, J. C.; Iyengar, S. S.; Tomasi, J.; Cossi, M.; Rega, N.; Millam, N. J.; Klene, M.; Knox, J. E.; Cross, J. B.; Bakken, V.; Adamo, C.; Jaramillo, J.; Gomperts, R.; Stratmann, R. E.; Yazyev, O.; Austin, A. J.; Cammi, R.; Pomelli, C.; Ochterski, J. W.; Martin, R. L.; Morokuma, K.; Zakrzewski, V. G.; Voth, G. A.; Salvador, P.; Dannenberg, J. J.; Dapprich, S.; Daniels, A. D.; Farkas, Ö.; Foresman, J. B.; Ortiz, J. V.; Cioslowski, J.; Fox, D. J. *Gaussian 09, Rev. C.01*; Gaussian Inc.: 2009.

(29) Thewalt, U.; Döppert, K.; Lasser, W. Darstellung und Struktur des Dreikernigen, Sauerstofften, Ionischen Cyclopentadienyl, Zirkonium Carboxylato Komplexes  $[\text{Zr}_3(\mu_3\text{-O})(\mu_2\text{-OH})_3(\mu_2\text{-C}_6\text{H}_5\text{COO})_3(\eta^5\text{-C}_5\text{H}_5)_3]^+\text{C}_6\text{H}_5\text{COO}^-\text{O}(\text{C}_2\text{H}_5)_2$ . *J. Organomet. Chem.* **1986**, *308*, 303.

(30) (a) Hunter, W. E.; Hrnrcr, D. C.; Vann Bynum, R.; Penttila, R. A.; Atwood, J. L. The Search for Dimethylzirconocene. Crystal Structures of Dimethylzirconocene, Dimethylhafnocene, Chloromethylzirconocene, and (p-Oxo) bis(methylzirconocene). *Organometallics* **1983**, *2*, 750–755. (b) Fachinetti, G.; Floriani, C.; Chiesi-Villa, A.; Guastini, C. Carbon Dioxide Activation. Deoxygenation and Disproportionation of Carbon Dioxide Promoted by Bis(cyclopentadienyl) titanium and -zirconium Derivatives. A Novel Bonding Mode of the Carbonato and a Trimer of the Zirconyl Unit. *J. Am. Chem. Soc.* **1979**, *101*, 1767–1775.

(31) Bai, G.; Roesky, H. W.; Lobinger, P.; Noltemeyer, M.; Schmidt, H.-G. Base-Assisted Formation of Organozirconium Oxides with the  $[\text{Zr}_6(\mu_6\text{-O})(\mu_3\text{-O})_8]$  Core Structure. *Angew. Chem., Int. Ed.* **2001**, *40*, 2156–2159.

(32) Bai, G.; Roesky, H. W.; Li, J.; Labahn, T.; Cimpoesu, F.; Magull, J. Synthesis, Structural Characterization, and Theoretical Treatment of an Unusual Organozirconium Hydroxide with the  $[\text{Zr}_6(\mu_4\text{-O})(\mu\text{-O})_4(\mu\text{-OH})_8]$  Core. *Organometallics* **2003**, *22*, 3034–3038.

(33) (a) Chi, Y.; Lan, J.-W.; Ching, W.-L.; Peng, S.-M.; Lee, G.-H. Syntheses and characterization of mixed acetylacetonate–catecholate complexes of zirconium,  $[\text{Zr}_3(\text{acac})_4(\text{cat})_4(\text{MeOH})_2]$ ,  $[\text{Zr}(\text{acac})_2(\text{DBcat})_2]$  ( $\text{H}_2\text{DBcat} = 3,5\text{-di-tert-butylcatechol}$ ) and  $[\text{Zr}_4(\mu_4\text{-O})(\text{acac})_4(\text{DBcat})_3(\text{OMe})_4(\text{MeOH})]$ . *J. Chem. Soc., Dalton Trans.* **2000**, 2923–2927. (b) Boyle, T. J.; Tribby, L. J.; Alam, T. M.; Bunge, S. D.; Holland, G. P. Catechol derivatives of group 4 and 5 compounds. *Polyhedron* **2005**, *24*, 1143–1152.

(34) Baumann, S. O.; Puchberger, M.; Schubert, U. Oximate-substituted zirconium alkoxides. *Dalton Trans.* **2011**, *40*, 1401.

(35) (a) Kickelbick, G.; Schubert, U. Oxozirconium Methacrylate Clusters:  $\text{Zr}_6(\text{OH})_4\text{O}_4(\text{OMc})_{12}$  and  $\text{Zr}_4\text{O}_2(\text{OMc})_{12}$  ( $\text{OMc} = \text{Methacrylate}$ ). *Chem. Ber.* **1997**, *130*, 473–477. (b) Puchberger, M.; Kogler, F.-R.; Jupa, M.; Gross, S.; Fric, H.; Kickelbick, G.; Schubert, U. Can the Clusters  $\text{Zr}_6\text{O}_4(\text{OH})_4(\text{OOCR})_{12}$  and  $[\text{Zr}_6\text{O}_4(\text{OH})_4(\text{OOCR})_{12}]_2$  Be Converted into Each Other? *Eur. J. Inorg. Chem.* **2006**, *2006*, 3283–3293.

(36) (a) Gigant, K.; Rammal, A.; Henry, M. Synthesis and Molecular Structures of Some New Titanium(IV) Aryloxides. *J. Am. Chem. Soc.* **2001**, *123*, 11632–11637. (b) Benedict, J. B.; Coppens, P. The Crystalline Nanocluster Phase as a Medium for Structural and Spectroscopic Studies of Light Absorption of Photosensitizer Dyes on Semiconductor Surfaces. *J. Am. Chem. Soc.* **2010**, *132*, 2938–2944. (c) Chaumont, C.; Mobian, P.; Henry, M. An unprecedented high nuclearity catecholobased Ti(IV)-architecture bearing labile pyridine ligands. *Dalton Trans.* **2014**, *43*, 3416–3419. (d) Chaumont, C.; Chaumont, A.; Kyritsakas, N.; Mobian, P.; Henry, M. Titanium oxo-clusters derivatized from the  $\text{Ti}_{10}\text{O}_{12}(\text{cat})_8(\text{py})_8$  complex: structural investigation and spectroscopic studies of light absorption. *Dalton Trans.* **2016**, *45*, 8760. (e) Yang, S.; Su, H.-C.; Hou, J.-L.; Luo, W.; Zou, D.-H.; Zhu, Q.-Y.; Dai, J. The effects of transition-metal doping and chromophore anchoring on the photocurrent response of titanium-oxo-clusters. *Dalton Trans.* **2017**, *46*, 9639. (f) Fan, X.; Fu, H.; Zhang, L.; Zhang, J. Pyrazole-thermal synthesis: a new approach towards N-rich titanium-oxo clusters with photochromic behaviors. *Dalton Trans.* **2019**, *48*, 8049. (g) Wang, H.; Zou, D.-H.; Jiang, G.-Q.; Dai, J. Cluster-to-cluster charge transfer in a compound with a co-crystallized dye-anchored  $\text{Ti}_6$  cluster and a classical  $\text{Ti}_{12}$  cluster. *Dalton Trans.* **2019**, *48*, 8569.

(37) Shi, C.; Zhang, M.; Hang, X.; Bi, Y.; Huang, L.; Zhou, K.; Xu, Z.; Zheng, Z. Assembly of thiocalix[4]arene-supported high-nuclearity  $\text{Cd}_{24}$  cluster with enhanced photocatalytic activity. *Nanoscale* **2018**, *10*, 14448–14454.

(38) (a) Miras, H. N. D.; Stone, D.; Long, L.; McInnes, E. J. L.; Kögerler, P.; Cronin, L. Exploring the Structure and Properties of Transition Metal Templated  $\{\text{VM}_{17}(\text{VO}_4)_2\}$  Dawson-Like Capsules. *Inorg. Chem.* **2011**, *50*, 8384–8391. (b) Xu, F.; Scullion, R. A.; Yan, J.; Miras, H. N.; Busche, C.; Scandurra, A.; Pignataro, B.; Long, D. L.; Cronin, L. A Supramolecular Heteropolyoxopalladate  $\{\text{Pd}_{15}\}$  Cluster Host Encapsulating a  $\{\text{Pd}_2\}$  Dinuclear Guest:  $[\text{Pd}^{\text{II}}_2\text{C}\{(\text{H}_7\text{Pd}_{15}\text{O}_{10})\text{O}_{10}(\text{PO}_4)_{10}\}]^{9-}$ . *J. Am. Chem. Soc.* **2011**, *133*, 4684–4686.

(39) (a) Wilson, E. F.; Miras, H. N.; Rosnes, M. H.; Cronin, L. Real-Time Observation of the Self-Assembly of Hybrid Polyoxometalates Using Mass Spectrometry. *Angew. Chem., Int. Ed.* **2011**, *50*, 3720–3724. (b) Miras, H. N.; Wilson, E. F.; Cronin, L. Unravelling the complexities of inorganic and supramolecular self-assembly in solution with electrospray and cryospray mass spectrometry. *Chem. Commun.* **2009**, No. 11, 1297–1311.

(40) Zang, H.; Surman, A.; Long, D.; Cronin, L.; Miras, H. N. Exploiting the equilibrium dynamics in the self-assembly of inorganic macrocycles based upon polyoxothiometalate building blocks. Exploiting the equilibrium dynamics in the self-assembly of inorganic macrocycles based upon polyoxothiometalate building blocks. *Chem. Commun.* **2016**, *52*, 9109–9112.

(41) (a) Zang, H. Y.; Chen, J. J.; Long, D. L.; Cronin, L.; Miras, H. N. Assembly of Thiometalate-Based  $\{\text{Mo}_{16}\}$  and  $\{\text{Mo}_{36}\}$  Composite Clusters Combining  $[\text{Mo}_2\text{O}_2\text{S}_2]^{2+}$  Cations and Selenite Anions. *Adv. Mater.* **2013**, *25*, 6245–6249. (b) Miras, H. N.; Zang, H. Y.; Long, D. L.; Cronin, L. Direct Synthesis and Mass Spectroscopic Observation of the  $\{\text{M}_{40}\}$  Polyoxothiometalate Wheel. *Eur. J. Inorg. Chem.* **2011**, *2011* (33), 5105–5111.

(42) Schleyer, P. v. R.; Manoharan, M.; Wang, Z.-X.; Kiran, B.; Jiao, H.; Puchta, R.; van Eikema Hommes, N. J. R. Dissected Nucleus-Independent Chemical Shift Analysis of  $\pi$ -Aromaticity and Anti-aromaticity. *Org. Lett.* **2001**, *3*, 2465–2468.

(43) Tsipis, A. C.; Depastas, I. G.; Tsipis, C. A. Diagnosis of the  $\sigma$ -,  $\pi$ - and  $(\sigma + \pi)$ -Aromaticity by the Shape of the NICS<sub>zz</sub>-Scan Curves and Symmetry-Based Selection Rules. *Symmetry* **2010**, *2*, 284–319.